ЖЭТФ, 2013, том 144, вып. 3 (9), стр. 519–551

JOSEPHSON VORTEX LATTICE IN LAYERED SUPERCONDUCTORS

A. E. Koshelev [a*], ***M. J. W. Dodgson*** [b]

[a] *Materials Science Division, Argonne National Laboratory 60439, Argonne, Illinois*

[b] *Theory of Condensed Matter Group, Cavendish Laboratory, Cambridge, CB3 0HE, UK*

Institut de Physique, Université de Neuchâtel 2000, Neuchâtel, Switzerland,

Department of Physics and Astronomy, University College London, London WC1E 6BT, UK

Received April 1, 2013

Dedicated to the memory of Professor Anatoly Larkin

Many superconducting materials are composed of weakly coupled conducting layers. Such a layered structure has a very strong influence on the properties of vortex matter in a magnetic field. This review focuses on the properties of the Josephson vortex lattice generated by the magnetic field applied in the direction of the layers. The theoretical description is based on the Lawrence–Doniach model in the London limit, which takes only the phase degree of freedom of the superconducting order parameter into account. In spite of its simplicity, this model leads to an amazingly rich set of phenomena. We review in detail the structure of an isolated vortex line and various properties of the vortex lattice, in both dilute and dense limits. In particular, we extensively discuss the influence of the layered structure and thermal fluctuations on the selection of lattice configurations at different magnetic fields.

DOI: 10.7868/S0044451013090071

1. INTRODUCTION

Layered superconductors are materials made from a stack of alternating thin superconducting layers separated by nonsuperconducting regions. The superconducting layers are essentially two-dimensional (2D) as long as they are so thin that there is no variation in fields, or in the superconducting order parameter, across each layer. Such structures frequently occur naturally in anisotropic crystals. A layered superconductor can carry supercurrents along the layers, as well as between the layers. This is due to the Josephson tunneling of Cooper pairs [1] across the insulating regions that separate neighboring superconducting layers, i. e., each pair of neighboring layers forms one Josephson junction. In general, the z-axis (Josephson) supercurrents are weaker than the supercurrents along the layers. A mere "layeredness" of atomic structure, however, does not automatically make a material a layered superconductor. When the interlayer electrical coupling is sufficiently strong, this discrete system of layers approximates to a continuous superconductor with uniaxial anisotropy. Hence, we are interested in the case where the approximation to a uniaxial continuous superconductor breaks down, which happens when the layer separation d is greater than the z-axis superconducting coherence length, $d \gg \xi_c$.

The most prominent example is the high-T_c cuprate superconductors, discovered in 1986 [2–5], which led to a huge interest in physics of layered superconductors. The two most studied cuprate compounds, $YBa_2Cu_3O_7$ (YBCO) and $Bi_2Sr_2CaCu_2O_x$ (BSCCO), have similar transition temperatures $T_c \approx 90$K and represent two important particular cases. YBCO is moderately anisotropic, with the anisotropy factor $\gamma \approx 5$–7, and its "layeredness" becomes essential at low temperatures when the c-axis coherence length ξ_c drops below the

*E-mail: koshelev@anl.gov

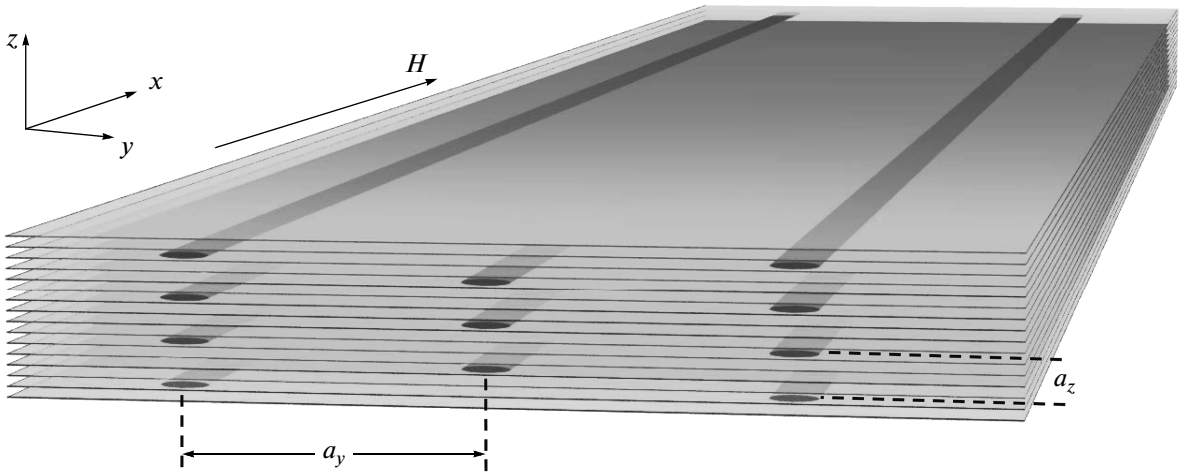

Fig. 1. Illustration of a dilute lattice of Josephson vortices generated in a layered superconductor by a magnetic field applied along the layer direction

layer spacing d. On the other hand, BSCCO has a huge anisotropy factor, $\gamma \approx 400 - 1000$, and behaves as a layered superconductor practically in the whole temperature range below T_c. Other naturally layered superconductors include the transition metal dichalcogenides [6, 7] and organic charge-transfer salts formed with the molecule BEDT-TTF [8, 9]. An important new family of atomically layered superconducting materials, iron pnictides and chalcogenides, was discovered in 2008 [10] and is being extensively explored since then (see, e. g., reviews [11–13]). Anisotropy of most compounds is actually not very high and they typically behave as anisotropic three-dimensional materials. There are important exceptions, however. The most studied compound in which the layered structure is clearly essential is $SmFeAsO_{1-x}F_x$ [14] with T_c up to 55 K. For example, the Josephson nature of the in-plane vortices at low temperatures has been recently demonstrated in this compound [15]. Also, several iron pnictide compounds with extremely high anisotropy have been discovered [16–18]. Properties of these compounds remain mostly unexplored due to their rather complicated composition.

All layered superconductors share a very similar general behavior of the vortex matter generated by an external magnetic field, which is insensitive to the microscopic nature of superconductivity inside the layers. Several excellent review articles have been published in the past covering different aspects of the vortex matter in type-II superconductors [19–23]. Nevertheless, we feel that further progress in the understanding of the Josephson vortices in layered superconductors warrants a specialized review, providing more details and discussing important recent results.

This short review narrowly focuses on the vortex lattice that appears at magnetic fields applied along the layers. In this case, the flux line winds its phase around an area between two neighboring layers and is called a Josephson vortex in analogy with a vortex in a superconducting tunneling junction. The Josephson vortex contains out-of-plane currents that tunnel via the Josephson effect from layer to layer. The current distribution around a vortex is anisotropic. As a consequence, the vortex lattice is also anisotropic: it is a triangular lattice strongly stretched along the layers (see Fig. 1). In addition, the restriction to lie between the layers leads to commensurability effects and an energy barrier to tilting the field away from the layers. There are two very different regimes depending on the magnetic field strength B_x. The crossover field scale B_{cr} separating these two regimes is set by the anisotropy factor γ and the layer periodicity d as $B_{cr} = \Phi_0/(2\pi\gamma d^2)$, where $\Phi_0 = hc/2e$ is the flux quantum. In the case of BSCCO, this field scale is around 0.5 tesla. In the dilute lattice regime, $B_x < B_{cr}$, the nonlinear cores of Josephson vortices are well separated and the distribution of currents and fields is very similar to that in continuous anisotropic superconductors [24]. The dense lattice regime is realized at high fields $B_x > B_{cr}$, where the cores of Josephson vortices overlap. In this regime, the Josephson vortices fill all layers homogeneously [25]. This state is characterized by rapid oscillations of the Josephson current and by very weak modulation of the in-plane current. In this re-

view, we characterize these two lattice regimes in more detail.

We do not consider the properties of vortices generated by a magnetic field applied perpendicular to the layers, along the c axis[1]. The structure of a c-axis vortex is very different from the structure of an in-plane vortex. In layered superconductors, a c-axis vortex can be viewed as a stack of weakly coupled pointlike pancake vortices. Properties of the pancake vortex lattice were also extensively explored, see, e. g., reviews [23] and [26] and the references therein.

Several experimental techniques have been employed to explore the Josephson vortex lattices. The dilute stretched lattice at small fields (< 100 G) has been directly observed in YBCO with Bitter decoration in [27], where the elliptical distribution of the flux around each Josephson vortex was also seen. At high fields (> 1 tesla), the commensurability between the c-axis parameter of the Josephson vortex lattice and the interlayer separation leads to magnetic field oscillations, which have been observed experimentally in underdoped YBCO in irreversible magnetization [28, 29] and nonlinear resistivity [30].

In much more anisotropic BSCCO, direct observation of Josephson vortices is not possible. However, when the magnetic field is tilted at small angles with respect to the layers, the c-axis field component generates the pancake-vortex stacks that preferably enter the superconductor along the Josephson vortices forming chains. Visualizing the flux of these chains, it is possible to find locations of vertical rows of the Josephson vortices and measure the in-plane lattice parameter a_y. This was done using a variety of visualization techniques, such as Bitter decorations [31, 32], scanning Hall probes [33], Lorentz microscopy [34, 35] and magnetooptical imaging [36, 37]. These observations have been summarized in review [38].

Most extensively, properties of the Josephson vortex lattice were explored in BSCCO using c-axis transport in small-size mesas [39–43]. These studies revealed a very rich dynamical behavior of the lattice, which is beyond the scope of this review. The very important feature is that, due to low dissipation, the Josephson vortex lattice can be accelerated up to very high velocities. It is clear that understanding dynamics is not possible without good understanding of static lattice properties. The dynamic phenomenon closely related to static lattice configurations is magnetic-field oscillations of resistance for very slow lattice motion, which have been discovered and explored in small-size BSCCO mesas [44–48]. The oscillation period can correspond to either the flux quantum or half the flux quantum per junction depending on the magnetic field and the lateral size of the mesa. An interplay between the bulk shearing interaction and the interaction with edges leads to very nontrivial evolution of lattice structures, which we consider in this review.

This review is organized as follows. We start in Sec. 2, where we present the energy functional and equilibrium equations for the phase and vector potential. In Sec. 3, we describe the structure and energetics of a single flux line. In Sec. 4, we discuss the dilute JVL and consider in detail the role of layered structure in selecting lattice configurations. The properties of the dense JVL at high fields are considered in Sec. 5. In this regime, the structure and energy of the lattice can be evaluated analytically using an expansion with respect to the Josephson coupling. In that section, we also review the magnetic field dependence of lattice configurations and oscillations of the critical current in finite-size samples. Elastic properties of both dilute and dense lattices are discussed in the corresponding sections. In Sec. 6, based on the elastic energies, we review effects caused by thermal fluctuations.

2. ENERGY FUNCTIONAL AND EQUATIONS FOR THE SUPERCONDUCTING PHASES AND VECTOR POTENTIAL

Theoretical analysis of the Josephson vortex matter in layered superconductors is based on a phenomenological model in which only the phase degree of freedom of the superconducting order parameters is taken into account and its amplitude variations are neglected,

$$F_{LLD}\left[\phi_n(\mathbf{r}_\parallel),\mathbf{A}(\mathbf{r})\right] = \int d^3r\frac{B^2}{8\pi} + \\ + \sum_n \int d^2r_\parallel \left\{\frac{E_0}{2}\left(\nabla_\parallel\phi_n + \frac{2\pi}{\Phi_0}\mathbf{A}_{\parallel,n}\right)^2 + \right. \\ \left. + \frac{E_J}{d^2}\left[1-\cos(\phi_{n+1}-\phi_n+\chi_{n,n+1})\right]\right\}, \quad (1)$$

where $E_0 = \Phi_0^2 d/(16\pi^3\lambda_{ab}^2)$ defines the in-plane phase stiffness and $E_J = E_0/\gamma^2 = \Phi_0^2 d/(16\pi^3\lambda_c^2)$ is the phase stiffness for smooth inter-layer phase variations, λ_{ab} and λ_c are the components of the London penetration depth, and $\gamma = \lambda_c/\lambda_{ab}$ is the anisotropy factor. The z component of the vector potential enters the tunnel-

[1] In the literature the layer plane and the axis perpendicular to the layers are frequently called "ab plane" and "c axis".

ing term in the form[2] $\chi_{n,n+1} = (2e/\hbar c)\int_{nd}^{(n+1)d} dz\, A_z$. Near the transition temperature, the above phase model can be obtained from the celebrated Lawrence–Doniach model [49] by fixing the order-parameter amplitude (London approximation). However, the model is actually more general and describes Josephson properties of a layered material in the whole temperature range. Starting from the phase model, a rich variety of lattice properties can be derived, which we review in this article.

Subject to some given boundary conditions, the configuration of $\{\phi_n, \mathbf{A}\}$ is determined by minimizing the free energy. This leads to a set of differential equations; for example, minimizing with respect to the phase gives the current-conservation condition

$$\nabla_\parallel^2 \phi_n + \frac{2\pi}{\Phi_0}\nabla_\parallel \cdot \mathbf{A}_{\parallel,n} = \\ = \frac{1}{(\gamma d)^2}\left(\sin\varphi_{n-1,n} - \sin\varphi_{n,n+1}\right), \quad (2)$$

with the gauge-invariant phase difference defined as $\varphi_{n,n+1} = \phi_{n+1} - \phi_n + \chi_{n,n+1}$. In this equation, the Josephson length $\Lambda_J = \gamma d$ appears for the first time. This length plays a very important role in layered superconductors because it determines the scale over which the phase can relax to minimize the Josephson coupling energy without costing too much energy in the gradient term. Three more equations result from minimizing with respect to the three components of the vector potential. We can write these in terms of the electric current density by using the Maxwell equation $\mathbf{j} = (c/4\pi)\nabla \times (\nabla \times \mathbf{A})$, which gives

$$\mathbf{J}_{\parallel,n} = -\frac{2\pi c E_0}{\Phi_0}\left(\nabla_\parallel \phi_n + \frac{2\pi}{\Phi_0}\mathbf{A}_{\parallel,n}\right), \quad (3)$$

$$J_{n,n+1} = -j_J \sin\varphi_{n,n+1}, \quad (4)$$

where $\mathbf{J}_{\parallel,n}$ is the 2D current density in the nth layer and $J_{n,n+1}$ is the current density in the $\hat{\mathbf{z}}$ direction between the nth and $(n+1)$th layers, which has the maximum value

$$j_J = \frac{2\pi c E_0}{\Phi_0 (\gamma d)^2}. \quad (5)$$

The four equations (2)–(4) are the starting point for finding the structure of vortices in layered superconductors. In fact, we can make the job of solving this set of equations slightly clearer by combining them into a differential equation for the gauge-invariant phase differences alone. This is done by using the general result

$$\frac{4\pi d}{c} J_{n,n+1} = \int_{nd}^{(n+1)d} dz\, [\nabla \times (\nabla \times \mathbf{A})]_z = \\ = \nabla_\parallel \cdot (\mathbf{A}_{\parallel,n+1} - \mathbf{A}_{\parallel,n}) - \frac{\Phi_0}{2\pi}\nabla_\parallel^2 \chi_{n,n+1}, \quad (6)$$

and combining this with (2) and (4) to arrive at

$$\nabla_\parallel^2 \varphi_{n,n+1} + \frac{1}{\lambda_c^2}\sin\varphi_{n,n+1} + \frac{1}{(\gamma d)^2} \times \\ \times \left[\sin\varphi_{n+1,n+2} - 2\sin\varphi_{n,n+1} + \sin\varphi_{n-1,n}\right] = 0. \quad (7)$$

Solving this equation then gives the entire solution for currents by using (4) to find $J_{n,n+1}$, and the conservation law

$$\nabla_\parallel \cdot \mathbf{J}_{\parallel,n} = J_{n,n+1} - J_{n-1,n} \quad (8)$$

to find $\mathbf{J}_{\parallel,n}$.

3. STRUCTURE OF A JOSEPHSON VORTEX IN A LAYERED SUPERCONDUCTOR

If we place a flux line directed along the layers, the singularity associated with the vortex core can be avoided by placing the center in the insulating layer between two superconducting layers (first noticed by Bulaevskii [50]). The structure of the "core" is similar to the structure of the phase drop across a flux line in a two-dimensional Josephson junction [51]. This well-studied problem has a solution where the phase difference across the two layers drops by 2π over a distance of the Josephson length Λ_J[3]. For the 3D layered superconductor, this length is given by $\Lambda_J = \gamma d$, and we can think of a central region γd wide and d high as the core of an in-plane vortex. Beyond this core, the flux density and currents are quite similar to those for a continuous anisotropic superconductor [24]. The screening by z-axis currents is much weaker than that by in-plane currents, and the flux line is stretched into an ellipsoidal shape with a large width $\sim \lambda_c$ along the layers. Even though only the "core" resembles the vortex in a 2D Josephson junction, it has become common in the literature to label the entire flux line with this orientation a Josephson vortex.

We now consider now a flux line directed along the x axis. The general structure of this Josephson vortex was first described by Bulaevskii [50]. The center

[2] Here e is chosen to be positive, $e > 0$, i. e., the charge of an electron is $-e$.

[3] This characteristic length was noted soon after the discovery of the Josephson effect [82].

of the vortex lies between two layers, such that there is no core with suppressed amplitude of the order parameter, while the structure at large distances from the center is similar to a conventional flux line. The phase around the vortex is not given trivially by symmetry, but is a solution of nonlinear equations (2). The most convenient path to a quantitative solution is to separate the problem into two different scales: At large scales, we can ignore the nonlinearity, and there is an analytic solution. At small scales, the numerical solution is simplified by ignoring the screening contribution of the vector potential. Fortunately, for $\lambda_{ab}/d \gg 1$, there is a large region of intermediate scales where both approximations work well, allowing us to match the small-scale and long-scale solutions.

We consider a vortex centered between layers 0 and 1, and $y = 0$, which is defined by the limiting values

$$\begin{aligned} &\phi_n(y) = 0, \text{ for } y \to +\infty, \\ &\phi_n(y) = \begin{cases} -\pi, & n \geq 1, \\ \pi, & n \leq 0, \end{cases} \quad \text{for } y \to -\infty. \end{aligned} \tag{9}$$

This corresponds to the following conditions for the interlayer phase difference:

$$\begin{aligned} &\varphi_{n,n+1} = 0, \text{ for } y \to \pm\infty \text{ and } n \neq 0, \\ &\varphi_{0,1} = \begin{cases} 0, & y \to +\infty, \\ -2\pi, & y \to -\infty. \end{cases} \end{aligned} \tag{10}$$

To obtain the current and field distributions, we first derive a useful exact equation for the magnetic field. The current components in (3) and (4) can be represented as

$$J_{n,n+1} = -\frac{c}{4\pi}\nabla_y B_x^{n,n+1} = -\frac{c\Phi_0}{8\pi^2\lambda_c^2 d}\sin\varphi_{n,n+1}, \tag{11}$$

$$J_{y,n} = \frac{c}{4\pi}\nabla_n B_x^{n-1,n} = \frac{c\Phi_0 d}{8\pi^2\lambda_{ab}^2}\left(\nabla_y\phi_n + \frac{2\pi}{\Phi_0}A_y\right), \tag{12}$$

where $B_x^{n,n+1}$ is the average magnetic field between the layers n and $n+1$ and ∇_n is a difference operator $\nabla_n A_n \equiv A_{n+1} - A_n$. Collecting the combination $(4\pi/c)\left(-\lambda_c^2\nabla_y J_{n,n+1} + (\lambda_{ab}^2/d)\nabla_n J_{y,n}\right)$, we obtain

$$\left[1 - \lambda_c^2\nabla_y^2 - (\lambda_{ab}^2/d^2)\nabla_n^2\right] B_x^{n,n+1} = \frac{\Phi_0}{2\pi d}\nabla_y\left(\varphi_{n+1,n} - \sin\varphi_{n+1,n}\right) \tag{13}$$

with $\nabla_n^2 A_n \equiv A_{n+1} + A_{n-1} - 2A_n$. The difference of $\varphi_{n+1,n}$ and $\sin\varphi_{n+1,n}$ decays outside the nonlinear core and satisfies the relation

$$\sum_n \int_{-\infty}^{\infty} dy \nabla_y \left(\varphi_{n+1,n} - \sin\varphi_{n+1,n}\right) = \sum_n \varphi_{n+1,n}\Big|_{-\infty}^{\infty} = 2\pi. \tag{14}$$

In the continuum limit, the right-hand side of (13) therefore converts into $\Phi_0\delta(y)\delta(z)$ and (13) transforms into the usual equation for the vortex magnetic field [52]

$$B_x - \lambda_c^2\nabla_y^2 B_x - \lambda_{ab}^2\nabla_z^2 B_x = \Phi_0\delta(y)\delta(z), \tag{15}$$

which gives

$$B_x = \frac{\Phi_0}{2\pi\lambda_c\lambda_{ab}} K_0\left(\sqrt{\left(\frac{y}{\lambda_c}\right)^2 + \left(\frac{z}{\lambda_{ab}}\right)^2}\right). \tag{16}$$

The current densities outside the core region are also given by standard formulas for anisotropic superconductors

$$j_y = -\frac{c\Phi_0}{8\pi^2\lambda_c\lambda_{ab}^2}\,\frac{z/\lambda_{ab}}{\sqrt{y^2/\lambda_c^2 + z^2/\lambda_{ab}^2}} \times K_1\left(\sqrt{\frac{y^2}{\lambda_c^2} + \frac{z^2}{\lambda_{ab}^2}}\right), \tag{17}$$

$$j_z = \frac{c\Phi_0}{8\pi^2\lambda_c^2\lambda_{ab}}\,\frac{y/\lambda_c}{\sqrt{y^2/\lambda_c^2 + z^2/\lambda_{ab}^2}} \times K_1\left(\sqrt{\frac{y^2}{\lambda_c^2} + \frac{z^2}{\lambda_{ab}^2}}\right). \tag{18}$$

These results should be valid as long as the linear approximation for the sine of the phase difference is good. To find the range of applicability for this approximation, we compare the last equation to (4), which near the vortex center, gives

$$\sin\varphi_{n,n+1} = -\frac{y/\gamma d}{(y/\gamma d)^2 + n^2} \quad \text{for } y^2/\lambda_c^2 + z^2/\lambda_{ab}^2 \ll 1, \tag{19}$$

indicating that the linear theory breaks down at $(y/\gamma d)^2 + n^2 \sim 1$. This condition therefore sets the boundary of the nonlinear core.

The above analysis shows that the Josephson vortex is characterized by two sets of length scales. A

region where the interlayer phase difference is large defines the nonlinear core of the vortex. In the z direction, this region is essentially localized within the central junction and in the y direction, it spreads over the Josephson length γd. At scales $|z|, |y|/\gamma \gg d$, the vortex structure is described by the anisotropic London theory. In addition, we can neglect screening effects in a wide region where the currents around the vortex decay as $1/r$ (although the current pattern is strongly stretched along the layers). Screening of the currents and magnetic field becomes important at the length scales $|z| \approx \lambda_{ab}$ and $|y| \approx \lambda_c$, which are much larger than the corresponding boundaries of the nonlinear core.

Due to this vortex structure, a quantitative analysis can be obtained with more ease by introducing an intermediate scale R_{int}, with $d < R_{int} < \lambda_{ab}$, such that at the distance $\sqrt{z^2 + (y/\gamma)^2} = R_{int}$ from the vortex center, both nonlinearity and screening may be ignored. We then consider the small-distance region $\sqrt{z^2 + (y/\gamma)^2} < R_{int}$ (containing the nonlinear core) and the large-distance region $\sqrt{z^2 + (y/\gamma)^2} > R_{int}$ (where screening will become important) separately. At small distances, we can neglect screening. In the London gauge $\nabla \cdot \mathbf{A} = 0$, this means that the vector potential $\mathbf{A}$ can be dropped and the vortex is described in terms of in- plane phases $\phi_n(y)$ only, which satisfy the equation (from (2))

$$(\gamma d)^2 \frac{d^2\phi_n}{dy^2} + \sin(\phi_{n+1} - \phi_n) - \\ - \sin(\phi_n - \phi_{n-1}) = 0 \quad (20)$$

and boundary conditions (9). These conditions are satisfied by our knowledge that outside the nonlinear core, where $(n - 1/2)^2 + (y/\gamma d)^2 \gg 1$, the phase has to approach the scaled version of the usual form relating to the angle around a vortex,

$$\phi_n^{Jv}(y) = -\operatorname{arctg}\left(\frac{\gamma d(n - 1/2)}{y}\right). \quad (21)$$

Multiplying (20) by $d\phi_n/dy$, summing over n, and performing an indefinite integral over y, we derive the following exact relation for all y:

$$\sum_n \left[(\gamma d)^2 \left(\frac{d\phi_n}{dy}\right)^2 - 2\left(1 - \cos(\phi_{n+1} - \phi_n)\right)\right] = \\ = \text{const}, \quad (22)$$

which is analogous to the first integral of a second-order differential equation with one variable. For an isolated Josephson vortex, the constant is zero. In contrast to the single-variable case, this relation does not help us to find the exact solution of coupled nonlinear equations (20), and we have either to use some approximate solution or to solve it numerically. Relation (22) can, however, be used to test the accuracy of the approximate and numerical solutions.

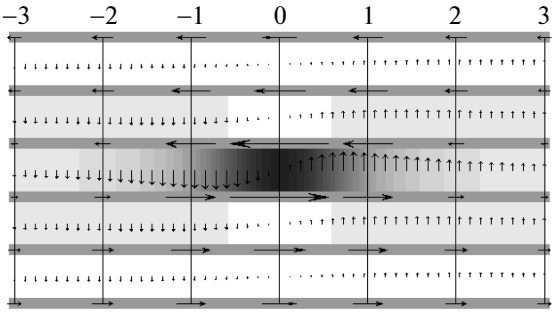

Fig. 2. Visualization of the numerically computed structure of an isolated Josephson vortex. The arrows represent the current distribution (half the interlayer distance corresponds to maximum Josephson current). The greylevel codes for the cosine of the interlayer phase difference. The scale in the y-direction is in units of the Josephson length $\Lambda_J = \gamma d$

A simple approximate solution has been proposed by Clem and Coffey [52] (the CC solution), who used the ansatz

$$B_x \approx \frac{\Phi_0}{2\pi\lambda_c\lambda_{ab}} K_0\left(\frac{\sqrt{y^2 + \gamma^2 z^2 + y_{cc}^2}}{\lambda_c}\right) \quad (23)$$

for the magnetic field and found that the best approximation for the core structure is achieved by selecting the cut off $y_{cc} = \gamma d/2$. This field distribution allows obtaining the distribution of the phase difference

$$\varphi_{n,n+1} \approx -\sin^{-1}\left\{\frac{d}{\lambda_{ab}} \frac{y}{R_n(y)} K_1\left(\frac{R_n(y)}{\lambda_c}\right)\right\}, \quad (24)$$

where $R_n(y) = \sqrt{y^2 + (\gamma dn)^2 + y_{cc}^2}$. In particular, at $\gamma d \ll y \ll \lambda_c$, this corresponds to $\phi_1(y) \approx \approx -\operatorname{tg}^{-1}(\gamma d/2y)$.

The accurate numerical structure for the core was obtained in Ref. [52]. Figure 2 presents a visualization of this numerical solution, and we compare the phase difference in the central junction to that from the CC solution in Fig. 3. The numerical solution is characterized by the following properties. The maximum in-plane phase gradient is given by

$$\gamma d \left.\frac{d\phi_1}{dy}\right|_{y=0} = 1.10 \quad (25)$$

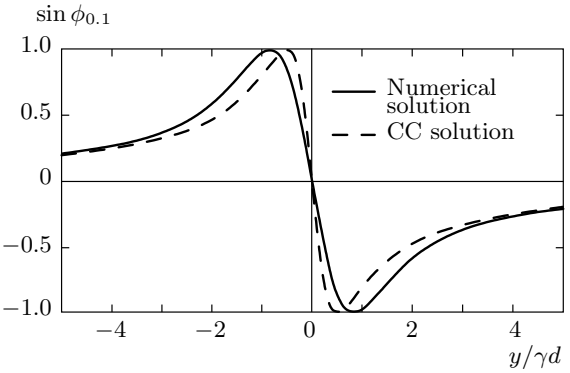

Fig. 3. Sine of the phase difference between the central layers of the Josephson vortex. For comparison, the approximate solution of Clem and Coffey [52] is also shown

(the CC solution gives $\gamma d\ (d\phi_1/dy)_{y=0} = 2$) and the maximum Josephson current flows at the distance $y_{max} = 0.84\gamma d$ from the vortex center (the CC solution gives $y_{max} = y_{cc} = 0.5\gamma d$). The maximum magnetic field in the vortex core is given by

$$B_x^{0,1}(y=0) \approx \frac{\Phi_0}{2\pi\lambda_c\lambda_{ab}}\left[\ln\left(\frac{\lambda_{ab}}{d}\right)+1.03\right]. \qquad (26)$$

The asymptotic limits for the phase difference in the central junction are

$$\varphi_{0,1} = \begin{cases} -\pi + \dfrac{2.20y}{\gamma d}, & |y| \ll \gamma d, \\ -\dfrac{\gamma d}{y}, & \gamma d \ll y \ll \lambda_c, \\ -\dfrac{d}{\lambda_{ab}}\sqrt{\dfrac{\pi\lambda_c}{2y}}e^{-y/\lambda_c}, & \lambda_c \ll y. \end{cases} \qquad (27)$$

Outside the core, we can calculate the correction $\delta\phi_n(y)$ to the continuum-limit phase asymptotics (21) by treating the discreteness and nonlinearity of the Josephson current perturbatively (see Appendix B). This gives

$$\delta\phi_n(y) = \frac{\sin[2\phi_n^{Jv}(y)]}{16\,R^2}\,(\ln R + C_{\delta\phi}) + \\ + \frac{5\sin[4\phi_n^{Jv}(y)]}{96\,R^2}, \qquad (28)$$

where $R = \sqrt{(n-1/2)^2 + (y/\gamma d)^2}$, and the constant $C_{\delta\phi} \approx 4.362$ is found from comparison with the numerical solution.

We can find the energy per unit length of the Josephson vortex by inserting this solution into (1). The simplest method [53] is again to split the energy into two contributions: one from the region at large distances where the linear approximation is valid, and one from small distances where we need the numerical solution, but can ignore the contributions of **A** to the current (i. e., ignore screening). The first is found analytically, while the second needs a numerical integration. The final result is (see also [54]),

$$\varepsilon_{Jv} = \frac{\varepsilon_0}{\gamma}\left[\ln\left(\frac{\lambda_{ab}}{d}\right)+1.55\right] \qquad (29)$$

with $\varepsilon_0 = \Phi_0^2/(4\pi\lambda_{ab})^2$. This energy determines the lower critical field $H_{c1,x}$ above which Josephson vortices are generated:

$$H_{c1,x} = 4\pi\varepsilon_{Jv}/\Phi_0 = \frac{\Phi_0}{4\pi\lambda_c\lambda_{ab}}\ln\left(\frac{0.44\lambda_{ab}}{d}\right). \qquad (30)$$

To summarize, the solution for a Josephson vortex presented here is very similar to the usual flux lines in isotropic superconductors, but stretched by the factor γ in the y-direction. The reason for this similarity is that the linear approximation to the Josephson relation works well away from the vortex center. The important feature, however, is that at the center of the vortex there is no normal core, but rather a phase drop of nearly 2π across the central junction over a distance of γd.

3.1. Line-tension energy of Josephson vortex

In this section, we consider the line-tension energy of a distorted Josephson vortex, an important parameter that determines thermal wandering of the vortex line and its response to pinning centers. We consider a kink-free vortex located in between the layers 0 and 1 and defined by the planar displacement field $u(x)$. Because the energy of the straight vortex does not depend on its orientation inside the layer plane, for very smooth distortions with the wavelength larger that λ_c, the line-tension energy is simply determined by the line energy in (29),

$$\delta F = \int dx \frac{\varepsilon_{Jv}}{2}\left(\frac{du}{dx}\right)^2 \text{ for } \left|\frac{du}{dx}\right| < \left|\frac{u}{\lambda_c}\right|.$$

This simple result, however, is of limited interest, because most properties of the vortex are determined by deformations with smaller wavelengths, $|du/dx|/|u| \sim \sim |k_x| \gg 1/\lambda_c$. In this range, the line-tension energy acquires nonlocality, a typical feature of vortex lines. An accurate calculation of the line tension for

this regime presented in Appendix A leads to the result

$$\delta F = \frac{\pi}{2}\varepsilon_J \int \frac{dk_x}{2\pi} k_x^2 \ln \frac{C_t}{\gamma d k_x} u^2 \qquad (31)$$

with $\varepsilon_J \equiv E_0/\gamma d$ and $C_t \approx 2.86$. The important feature is the logarithmic dependence of the effective line tension on the deformation wave vector, which is a consequence of nonlocality.

4. DILUTE LATTICE, $B_x < \Phi_0/2\pi\gamma d^2$

When the Josephson vortices are well separated, the linear and continuous approximation can be applied to energy functional (1) everywhere except in the core regions, which reduces it to the anisotropic London model

$$F_L\left[\phi(\mathbf{r}), \mathbf{A}(\mathbf{r})\right] \approx \int d^3r \left\{ \frac{B_x^2}{8\pi} + \frac{E_0}{2} \times \right.$$
$$\times \left[\left(\nabla_\parallel \phi + \frac{2\pi}{\Phi_0} \mathbf{A}_\parallel \right)^2 + \right.$$
$$\left. \left. + \frac{1}{\gamma^2} \left(\nabla_z \phi + \frac{2\pi}{\Phi_0} A_z \right)^2 \right] \right\}. \qquad (32)$$

This means that the lattice solution is just a linear addition of single flux-line solutions and the lattice energy is determined by this London model. To understand the nature of the ground state, it is useful to apply the rescaling trick [55, 56]

$$\tilde{\mathbf{r}} = (y, \gamma z) \text{ and } \tilde{\mathbf{A}} = (A_y, A_z/\gamma), \qquad (33)$$

which in the case of zero z-component of the magnetic field precisely reduces the system to the isotropic state [24]. Therefore, the ground state configuration in scaled coordinates is given by a regular triangular lattice. In real coordinates, this state corresponds to the triangular lattice strongly stretched along the direction of the layers.

Within the anisotropic London model, the lattice is degenerate with respect to rotation in scaled coordinates. In real coordinates, this corresponds to an "elliptic rotation" illustrated in Fig. 4. In particular, there are two aligned configurations, in which Josephson vortices form vertical stacks along the z axis (see Fig. 5). For these configurations, the vertical distance between the Josephson vortices in the stacks, a_z, and the separation between the stacks, a_y, are given by

$$a_z = \sqrt{\beta\Phi_0/(\gamma B_x)},\ a_y = \sqrt{\gamma\Phi_0/(\beta B_x)}, \qquad (34)$$

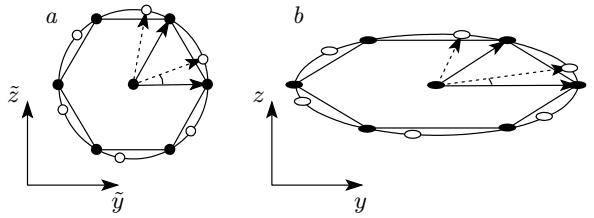

Fig. 4. Ground-state lattice configuration for an in-plane field and its rotational degeneracy within the anisotropic London model in (a) scaled coordinates and (b) real coordinates. The ellipse aspect ratio corresponds to the anisotropy factor ≈ 3, much smaller, e. g., than the anisotropy of BSCCO

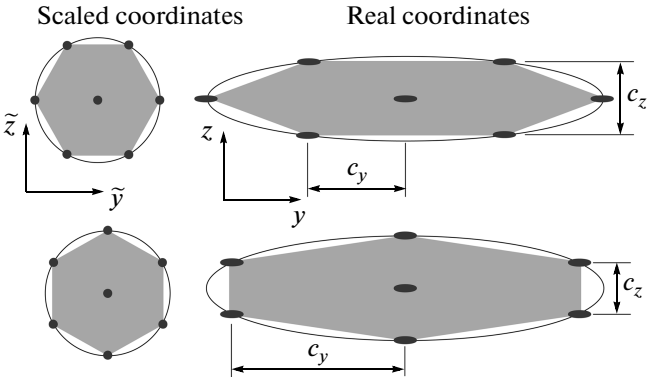

Fig. 5. The two alternative lattice configurations that are aligned with the layers, in scaled and real coordinates

where the constant β is respectively equal to $2\sqrt{3}$ and $2/\sqrt{3}$ for the upper and lower configuration in Fig. 5.

The interaction energy of the Josephson vortex lattice can be reduced to the interaction energy of an Abrikosov vortex lattice using the scaling trick. This energy must be added to the self energy of each Josephson vortex (29), which, in the intermediate field regime $H_{c1,x} \ll \overline{B}_x \ll B_{\gamma d^2}$, gives the result

$$f_{JI} \approx \frac{\overline{B}_x^2}{8\pi} + \frac{\overline{B}_x}{\Phi_0} \frac{\varepsilon_0}{2\gamma} \ln \left(\frac{1.23\Phi_0}{\gamma d^2 \overline{B}_x} \right). \qquad (35)$$

The "elliptic rotation" degeneracy is eliminated by the layered structure of the superconductor. There are several different mechanisms of this elimination. First, due to the strong intrinsic pinning, the vortex centers must be located in between the layers. This limits the possible lattice orientations. A second, less trivial, mechanism is from the corrections due to the discrete lattice structure to the vortex interactions. The degeneracy is also eliminated by thermal fluctuations,

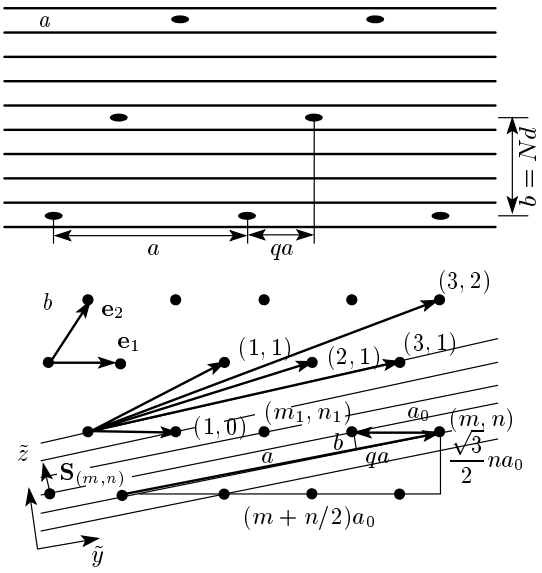

Fig. 6. (a) General Josephson vortex lattice and its parameters. (b) Orientation of a layered structure with respect to the ideal lattice (in scaled coordinates). The layered structure fits the ideal lattice only if it is oriented along one of the crystallographic directions, which is characterized by two numbers (m, n), corresponding to the expansion of the direction vector over the two basic lattice vectors $\mathbf{e}_1$ and $\mathbf{e}_2$. Several possible directions are shown with the corresponding indices (m, n). The layers, together with the lattice parameters a, b, and q, are drawn here for the $(3, 1)$ orientation

because Josephson vortices mostly fluctuate along the layer directions and this selects preferential lattice orientations. All these mechanisms are considered in detail below.

4.1. Selection of ground-state configurations by the layered structure

As the centers of the Josephson vortices must be located between the layers, the layered structure plays a crucial role in the selection of the ground-state lattice configurations. The Josephson-vortex lattice is commensurate with the layered structure only at a discrete set of magnetic fields. Due to the "elliptic rotation" degeneracy of the lattice within the London approximation, the family of commensurate lattices includes lattices aligned with the layers (see Fig. 5), as well as misaligned ones. To make a full classification of commensurate lattices, we consider a general lattice shown in Fig. 6*a* [57, 58]. The lattice is characterized by three parameters: the in-plane period a, the distance between vortex rows in the z direction $b = Nd$, and the relative shift between the neighboring vortex rows in qa. The lattice shape is characterized by two dimensionless parameters, q and the ratio $r = b/a$. The lattice parameters are related to the in-plane magnetic field B_x as $B_x = \Phi_0/(ab)$. The two aligned structures in Fig. 5 correspond to $q = 1/2$. As the replacement $q \to 1 - q$ corresponds to a mirror reflection with respect to the xz plane, every structure with $q \neq 1/2$ is doubly degenerate. In addition to giving the general ground states, these lattices describe multiple metastable states with unique properties studied in Refs. [57, 58], which we review below.

We now classify the exactly commensurate lattices to give the set of commensurate fields. An equivalent geometrical analysis has been done in Ref. [59] following a somewhat different line of reasoning, but with the same final result for the commensurate fields. The analysis of commensurability conditions can be done most conveniently in scaled coordinates (33). In these coordinates, the ground-state configuration corresponds to a regular triangular lattice with the period $\tilde{a}_\Delta = \sqrt{2\gamma\Phi_0/\sqrt{3}B_x}$. It is convenient to consider the orientation of the layered structure with respect to this lattice rather than vice versa. The layered structure fits this lattice only if it runs along one of the crystallographic directions (see Fig. 6*b*). This direction (m, n) is defined by the lattice vector $\mathbf{e}_{m,n}$, which can be expanded over the two basic lattice vectors: $\mathbf{e}_{(m,n)} = m\mathbf{e}_1 + n\mathbf{e}_2$. For nonequivalent directions, m and n must be relatively prime numbers (i. e., there is no integer other than one that divides both m and n). Any such direction corresponds to a set of matching fields, denoted by $B_{(m,n)}(N)$. We also let $a_{(m,n)}$, $b_{(m,n)}$, and $q_{(m,n)}$ denote the lattice parameters corresponding to such an orientation. Immediately, we obtain

$$a_{(m,n)} = e_{(m,n)} = \tilde{a}_\Delta \sqrt{m^2 + mn + n^2}. \qquad (36)$$

It is useful to write the unit vector $\hat{\mathbf{z}}$ perpendicular to the layers in terms of $\mathbf{e}_{(m,n)}$. This vector is labelled $\mathbf{s}_{(m,n)}$ in Fig. 6*b* and is given by

$$\mathbf{s}_{(m,n)} \equiv \hat{\mathbf{z}} = \frac{\mathbf{e}_{(m,n)} \times \hat{\mathbf{x}}}{e_{(m,n)}}. \qquad (37)$$

Commensurability means that the projections of the two basic lattice vectors on $\mathbf{s}_{(m,n)}$ must be integer multiples of the number of layers, i. e.,

$$\mathbf{e}_1 \cdot \mathbf{s}_{(m,n)} = \tilde{n}\gamma d, \quad \mathbf{e}_2 \cdot \mathbf{s}_{(m,n)} = \tilde{m}\gamma d, \qquad (38)$$

(in scaled coordinates, the interlayer distance is γd). Using (36) and (37), we rewrite these conditions as

$$\frac{\sqrt{3}}{2}\tilde{a}_\Delta \frac{n}{\sqrt{m^2+mn+n^2}} = \tilde{n}\gamma d, \tag{39}$$

$$\frac{\sqrt{3}}{2}\tilde{a}_\Delta \frac{m}{\sqrt{m^2+mn+n^2}} = \tilde{m}\gamma d. \tag{40}$$

These equations mean that $\tilde{m}/\tilde{n} = m/n$. Because m and n are by definition relatively prime, the set of allowed $\tilde{m}$ and $\tilde{n}$ is simply given by $\tilde{m} = Nm$ and $\tilde{n} = Nn$. Therefore, we can represent the commensurability condition as

$$\frac{\sqrt{3}}{2}\tilde{a}_\Delta = N\sqrt{m^2+mn+n^2}\gamma d, \tag{41}$$

which gives the following set of commensurate fields, distances between neighboring rows $b = Nd$, and ratios $r_{(m,n)}$:

$$B_{(m,n)}(N) = \frac{\sqrt{3}}{2}\frac{\Phi_0}{N^2\gamma d^2(m^2+mn+n^2)}, \tag{42}$$

$$b_{(m,n)} = \frac{\frac{\sqrt{3}}{2}\tilde{a}_\Delta}{\sqrt{m^2+mn+n^2}}, \tag{43}$$

$$r_{(m,n)} = \frac{\sqrt{3}/2}{m^2+mn+n^2}. \tag{44}$$

Finding the parameter $q_{(m,n)}$ for a general orientation is a more complicated problem. Defining the direction to the nearest-row site (m_1, n_1) (see Fig. 6), we have

$$q_{(m,n)} = \frac{\mathbf{e}_{(m,n)}\cdot\mathbf{e}_{(m_1,n_1)}}{|\mathbf{e}_{(m,n)}|^2} = \\ = \frac{|mm_1 + (m_1n+mn_1)/2 + nn_1|}{m^2+mn+n^2}. \tag{45}$$

Expressing the neighboring-row separation via (m_1, n_1),

$$b_{(m,n)} = \frac{|[\mathbf{e}_{(m,n)}\times\mathbf{e}_{(m_1,n_1)}]|}{e_{(m,n)}} = \frac{\frac{\sqrt{3}}{2}\tilde{a}_\Delta|m_1n-mn_1|}{\sqrt{m^2+mn+n^2}}$$

and comparing it with Eq. (43), we can see that the pair (m_1, n_1) must satisfy the condition

$$|m_1n - mn_1| = 1. \tag{46}$$

It is well known from the theory of numbers that for any relatively prime pair (m, n), there exists a complementary pair (m_1, n_1) satisfying this condition, and there is a general recipe to find complementary pairs based on the Euclid algorithm (see, e. g., Ref. [60]). Moreover, because the combination $m_1n - mn_1$ does not change under the substitution $m_1 \to m_1 + m$, $n_1 \to n_1 + n$, there is an infinite set of pairs that satisfy condition (46) (physically, this corresponds to different lattice sites in the neighboring row). Therefore, the problem to find $q_{(m,n)}$ can be formulated as follows: among all pairs (m_1, n_1) satisfying condition (46), find the pair that minimizes $|mm_1 + (m_1n + mn_1)/2 + nn_1|$ and use this pair in Eq. (45). (Practically, we need not search to very high-order directions.) In the case $n = 1$ and arbitrary m, the choice of (m_1, n_1) is obvious, $(m_1, n_1) = (-1, 0)$, and we obtain

$$q_{(m,1)} = \frac{m+1/2}{m^2+m+1}. \tag{47}$$

We stress that these results essentially rely on the linear London approximation, which implies a very strong inequality $\tilde{a}_\Delta \gg \gamma d$, or equivalently, $N\sqrt{m^2+mn+n^2} \gg 1$. The number of vortex-free layers per unit cell is given by $N - 1$. The case $N = 1$ represents a special situation where all the layers are filled with vortices and are equivalent. It is interesting to note that even for a dilute lattice, we can have Josephson vortices in every layer ($N = 1$) in the case of high-order commensurability ($m, n \gg 1$). In an ideal situation, the lattice transfers with changing the magnetic field between different commensurate configurations via a series of first-order phase transitions. The number of competing states rapidly increases as the field decreases.

A full analysis of the structural evolution requires consideration of the energy. In the London limit, a very useful expression for the energy of the general lattice in Fig. 6*a* has been derived in Ref. [60]. We outline this derivation and present the final result in a somewhat different form. For the lattice in Fig. 6*a*, the interaction energy in the London limit is given by

$$f_{Jl}^{int} = \frac{B_x^2}{8\pi}\times \\ \times\left[\sum_{l,k}\left\{1+\lambda_{ab}^2\left[\frac{\gamma^2}{a^2}(2\pi l)^2 + \left[\frac{2\pi}{b^2}(k-ql)\right]^2\right]\right\}^{-1} - \right. \\ \left. - \int dy\,dz\left\{1+\lambda_{ab}^2\left[\frac{\gamma^2}{a^2}(2\pi z)^2 + \frac{(2\pi y)^2}{b^2}\right]\right\}^{-1}\right].$$

Using the formula

$$\sum_{k=-\infty}^{\infty} \frac{1}{(k+v)^2+u^2} = \frac{\pi}{u}\frac{\mathrm{sh}\,(2\pi u)}{\mathrm{ch}\,(2\pi u)-\cos(2\pi v)}$$

we can sum over k and integrate over y, leading to

$$f_{Jl}^{int} = \frac{B_x^2}{8\pi}\frac{b^2}{2\pi\lambda_{ab}^2}\left[\frac{\pi\lambda_{ab}}{b}\frac{\mathrm{sh}\,(b/\lambda_{ab})}{\mathrm{ch}\,(b/\lambda_{ab})-1} + \right.$$
$$\left. + \sum_{l=1}^{\infty}\frac{1}{g_b(l)}\frac{\mathrm{sh}\,[2\pi g_b(l)]}{\mathrm{ch}\,[2\pi g_b(l)]-\cos(2\pi q l)} - \int_0^{\infty} dz \frac{1}{g_b(z)}\right]$$

with $g_b(z) = \sqrt{(b/2\pi\lambda_{ab})^2 + r^2 z^2}$ and $r = b\gamma/a$. This expression significantly simplifies in the intermediate region $b \ll 2\pi\lambda_{ab}$, where we can use the expansion

$$\frac{\pi\lambda_{ab}}{b}\frac{\mathrm{sh}\,(b/\lambda_{ab})}{\mathrm{ch}\,(b/\lambda_{ab})-1} \approx \frac{2\pi\lambda_{ab}^2}{b^2} + \frac{\pi}{6}$$

and drop $b^2/(2\pi\lambda_{ab})^2$ in $g_b(z)$ meaning that $g_b(z) \to$ $\to rz$. This allows us to represent the interaction energy in this regime as [57]

$$f_{Jl}^{int} = \frac{B_x^2}{8\pi} + \frac{B_x\Phi_0}{(4\pi)^2\lambda_{ab}\lambda_c} \times$$
$$\times \left[\frac{1}{2}\ln\left(\frac{\Phi_0}{2\pi\lambda_{ab}\lambda_c B_x}\right) + \gamma_E - \ln 2 + G_L(r,q)\right] \quad (48)$$

with $\gamma_E = 0.5772$ being the Euler constant and

$$G_L(r,q) = \frac{\pi r}{6} + \sum_{l=1}^{\infty}\frac{\cos(2\pi q l) - \exp(-2\pi r l)}{l[\mathrm{ch}\,(2\pi r l) - \cos(2\pi q l)]} -$$
$$- \frac{1}{2}\ln(2\pi r). \quad (49)$$

The dimensionless function $G_L(r,q)$ depends only on the lattice shape. Its absolute minimum corresponding to the triangular lattice is given by $G_L(\sqrt{3}/2, 1/2) =$ $= -0.4022$. A peculiar property of $G_L(r,q)$, following from the rotational degeneracy, is that this function also has this value for the whole set of pairs $(r,q) = (r_{(m,n)}, q_{(m,n)})$ corresponding to the different lattice orientations. In particular, for $(m,n) = (m,1)$, we have

$$G_L\left(\frac{\sqrt{3}/2}{m^2+m+1}, \frac{m+1/2}{m^2+m+1}\right) = G_L\left(\sqrt{3}/2, 1/2\right).$$

This function also has very peculiar behavior at small r, which is important for the statistics of metastable states [58]: at $r \to 0$ it acquires peaks at all rational values of $q = k/l$. Large-order peaks with the denominator l develop as r drops below $1/(2\pi l)$.

For layered superconductors, we have

$$b = Nd, \quad a = \frac{\Phi_0}{B_x dN}, \quad r = N^2\frac{B_x}{B_{\gamma d^2}}$$

with $B_{\gamma d^2} = \Phi_0/(\gamma d^2)$ and, adding the energy of isolated Josephson vortices, we can write the total energy of the lattice as

$$f_{Jl}(N,q,h) = \frac{B_x^2}{8\pi} +$$
$$+ \frac{B_x\Phi_0}{(4\pi)^2\lambda_{ab}\lambda_c}\left[\frac{1}{2}\ln\left(\frac{1}{h}\right) + 1.432 + G_L(r,q)\right] \quad (50)$$

with $h \equiv 2\pi B_x/B_{\gamma d^2}$ and $r = N^2 h/2\pi$. For a given h, the ground state configuration is determined by the minimum of $G_L(N^2h/2\pi, q)$ with respect to discrete N and continuous q. As follows from Eq. (42), perfect fits where G_L reaches its absolute minimum occur at the set of reduced fields $h = h_{(m,n)}(N)$, where

$$h_{(m,n)}(N) = \frac{\sqrt{3}\pi}{N^2(m^2+mn+n^2)}. \quad (51)$$

At these fields, this energy reproduces the result in (35). The field dependence of G_L for the ground state is shown in Fig. 7. The continuous London model does not not accurately describe layered superconductors at high fields. To obtain lattice structures in this region, one has to consider the more general Lawrence–Doniach model. The transition between the aligned lattices have been studied within this model by Ichioka [61]. However, our analysis in the next section shows that at many fields, the true ground state is not given by an aligned lattice.

4.2. Evolution of ground-state configurations within the Lawrence–Doniach model

The accurate analysis of lattice configurations within the Lawrence–Doniach model which we report in this section was only published in short proceeding [62]. Independently, such numerical analysis was done by Nonomura and Hu [63], with fully consistent results.

At high in-plane magnetic fields, the spatial variations of the field are very small and can be neglected in the first approximation. In this limit, the only relevant degrees of freedom are the superconducting phases and

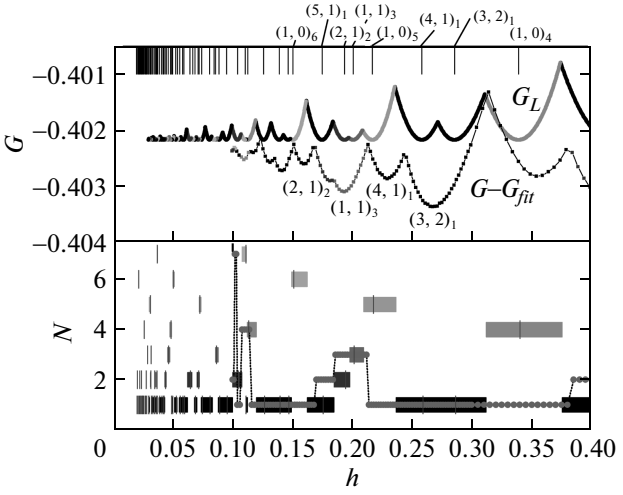

Fig. 7. Upper panel: The field dependence of the reduced energy functions for the London model (G_L, upper curve) and the full Lawrence–Doniach model ($G - G_{fit}$, lower curve). For clearer comparison, we subtracted from $G(h)$ its fit at small h given by Eq. (58). Values of commensurate fields $h_{(m,n)}(N)$ are shown in the top axis and the corresponding indices for several of them are written in the format $(m,n)_N$. As expected, G_L reaches its absolute minimum for every $h_{(m,n)}(N)$. The lower panel shows the field dependence of N for the ground state for both models (stripes for the London model and circles for the Lawrence–Doniach model). The same grey level codes the value of N in the upper panel and the London-model plot in the lower panel

the relevant part of LLD energy (1) per unit volume, $f_\phi \equiv F_{LLD}/(L_x L_y L_z) - B_x^2/(8\pi)$, can be written as

$$f_\phi[\phi_n(\mathbf{r})] = \frac{E_0}{L_y L_z}\sum_n \int dy \left[\frac{1}{2}\left(\nabla_y \phi_n\right)^2 + \right.$$
$$\left. + \frac{1}{(\gamma d)^2}\left(1 - \cos\left(\phi_{n+1} - \phi_n + \frac{2\pi d B_x y}{\Phi_0}\right)\right)\right]. \quad (52)$$

To simplify the analysis, we introduce the reduced in-plane length $\bar{y} \equiv y/\gamma d$ and the reduced magnetic field $h \equiv 2\pi\gamma d^2 B_x/\Phi_0$, which yields

$$f_\phi[\phi_n(\mathbf{r})] = \frac{\varepsilon_J}{L_y L_z}\sum_n \int d\bar{y} \left[\frac{1}{2}\left(\nabla_{\bar{y}} \phi_n\right)^2 + \right.$$
$$\left. + 1 - \cos\left(\phi_{n+1} - \phi_n + h\bar{y}\right)\right] \quad (53)$$

with $\varepsilon_J \equiv E_0/\gamma d$. Varying this energy with respect to the phases $\phi_n(\bar{y})$, we obtain an equation for the equilibrium phase distribution (equivalent to (2) when we ignore the spatial dependence in B_x):

$$\nabla_{\bar{y}}^2 \phi_n + \sin\left(\phi_{n+1} - \phi_n + h\bar{y}\right) -$$
$$- \sin\left(\phi_n - \phi_{n-1} + h\bar{y}\right) = 0. \quad (54)$$

We again consider a general lattice shown in Fig. 6*a* with the in-plane period a, with N layers between neighboring rows, and with the relative shift qa between relative rows, where a and N are related to the reduced field as $h = 2\pi\gamma d/Na$. It is sufficient to find the solution for the phase in one unit cell, $0 < y < a$, $1 \le n \le N$, using appropriate quasiperiodicity conditions for the phase. The total lattice energy per unit volume can be represented as

$$f_\phi = \frac{B_x \Phi_0}{(4\pi)^2 \lambda_{ab}\lambda_c} u(N,q,h), \quad (55)$$

where the reduced energy $u(N,q,h)$ per unit cell is given by

$$u(N,q,h) = \frac{1}{\pi}\sum_{n=1}^{N}\int_0^a d\bar{y} \times$$
$$\times \left[\frac{1}{2}\left(\frac{d\phi_n}{d\bar{y}}\right)^2 + 1 - \cos\left(\phi_{n+1} - \phi_n + h\bar{y}\right)\right]. \quad (56)$$

Using a relaxation method to solve (54) numerically within one unit cell, we can find the energy u for any given values of N, q and h. To match London representation (48), we write $u(N,q,h)$ in the form

$$u(N,q,h) = \frac{1}{2}\ln\frac{1}{h} + 1.4323 + G(N,q,h) \quad (57)$$

where the function $G(N,q,h)$ defined by this equation approaches the London limit $G_L(r = N^2 h/2\pi, q)$ as $h \to 0$.

We first consider the influence of the layered structure at small fields. As shown in Appendix B, in the lowest order with respect to h, the layered structure gives an orientation-independent correction to energy, $G \approx (h/32)\ln(C_h/h)$. In the higher (quadratic) order, the layered structure generates an orientation-dependent correction to the lattice energy, leading to a breakdown of the "elliptic-rotation" degeneracy of the lattice. To study this effect quantitatively, in Fig. 8, we plot the computed field dependences of $G(N,q,h)$ for several lattice orientations at the corresponding reduced commensurate fields $h_{(m,n)}(N)$ given by (51). At small h, $h < 0.05$, neglecting a very weak dependence

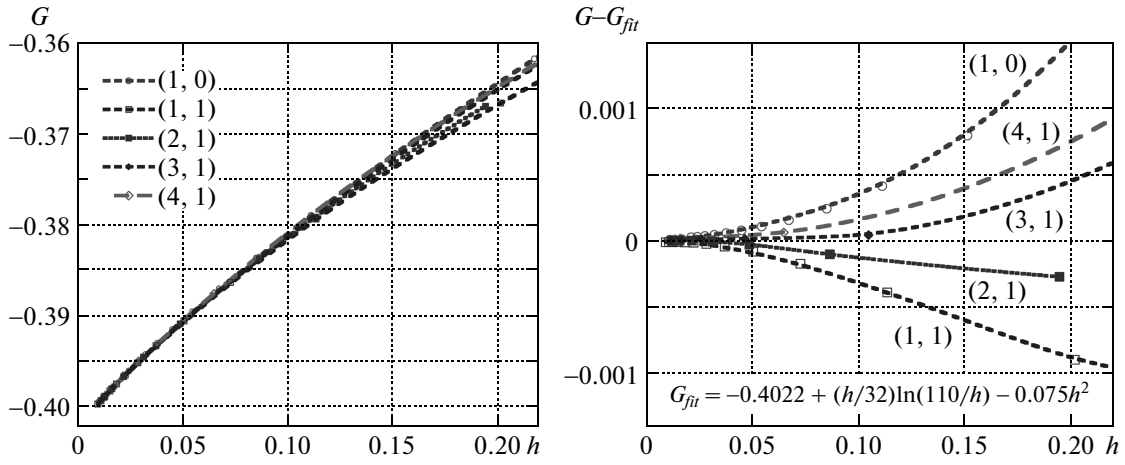

Fig. 8. Left panel: Field dependence of the reduced-energy function $G(N, h, q)$ for several lattice orientations (m, n) at the commensurate field $h_{(m,n)}(N)$. In the right panel, to enlarge small differences, we plot the difference between G and its fit obtained using all data for $h < 0.05$

on orientation, we can accurately fit the correction from the layeredness as

$$G(h) - G_L \approx \frac{h}{32} \ln \frac{110}{h} - 0.075h^2. \qquad (58)$$

It follows that among the two aligned structures shown in Fig. 5, the layers favor the lower structure with indices $(1, 1)$. However, for $h < 0.1$, the energy difference between the two structures is tiny and external factors may select the lattice orientation in real samples. On the other hand, we can expect that at sufficiently large fields, the ground-state configuration is selected by the layered structure even in real samples.

Energy corrections due to the layered structure favor lattice stretching along the layer direction and shift down the matching fields. This effect is strongest for the aligned lattice (1,0) and is illustrated in Fig. 9. In this figure, we show the field dependences of $G(N, h, 0.5)$ for different N. When a smooth function is subtracted from these dependences, local minima are realized at fields $\tilde{h}_{(1,0)}(N)$ that are smaller than the London matching field $h_{(1,0)}(N)$. The shift $\tilde{h}_{(1,0)}(N) - h_{(1,0)}(N)$ rapidly decreases with increasing the magnetic field. We found that this shift is described by the equation

$$\tilde{h}_{(1,0)}(N) \approx \frac{h_{(1,0)}(N)}{1 + (0.63/N^2) \ln(19/\tilde{h}_{(1,0)}(N))}.$$

For other lattice orientations, the shift is smaller but still noticeable. To quantify the energy difference between the aligned lattices due to the layered structure,

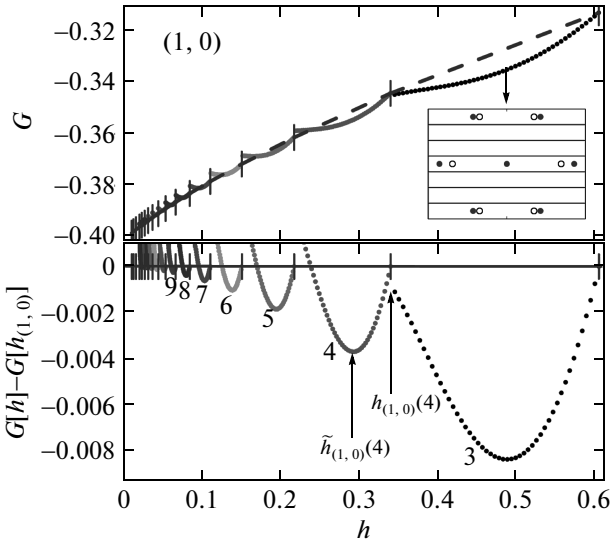

Fig. 9. Upper panel: The field dependences of the reduced-energy function $G = G(N, h, 0.5)$ for the aligned lattice $(1, 0)$ and different N. Vertical bars mark locations of the London-model commensurate fields $h_{(1,0)}(N)$. Lower panel shows the difference between $G(N, h, 0.5)$ and a smooth curve through the points $(h_{(1,0)}(N),\ G(N, h_{(1,0)}(N), 0.5))$ (dashed line in the upper panel). We can see that the matching fields are systematically displaced to the lower values $\tilde{h}_{(1,0)}(N)$, as illustrated for $N = 4$. The inset in the upper panel shows the lattice structure at the displaced matching field for $N = 3$ (solid symbols) in comparison with the regular-hexagon structure at the London matching field

we fit their energies at the shifted matching field for $h < 0.1$ to smooth curves and subtract these curves. This procedure gives $G_{(1,1)} - G_{(1,0)} \approx -0.011h^2$.

We can now explore the evolution of the ground-state configuration by direct minimization of the energy with respect to the lattice parameters N and q defined in Fig. 6. For this, we have computed the reduced ground-state energy defined as $G(h) \equiv \equiv \min_{N,q}[G(N,q,h)]$. We checked that if we consider only aligned lattices, the results of Ichioka [64] are reproduced for the transition fields between lattices with different periods N in the case of large anisotropy. For comparison, we also made a similar calculation for the London model and computed the field dependence of the function $G_L(h) = \min_{N,q}[G_L(r = N^2h/(2\pi), q)]$ where $G_L(r,q)$ is defined in Eqs. (48) and (49). In Fig. 7, we compare field evolutions of these ground-state reduced energies and the corresponding c-axis period N. For clearer comparison, we subtracted from $G(h)$ its fitted correction from $G_L(\sqrt{3}/2, 1/2)$ at small h given in (58). Values of the London commensurate fields $h_{(m,n)}(N)$ are shown on the top axis with several low-order fields marked by corresponding indices using the format $(m,n)_N$. As expected, $G_L(h)$ reaches its absolute minimum for every $h_{(m,n)}(N)$. We can observe several interesting properties. Because the lattice orientation with indices $(m,n) = (1,0)$ is not favored by the layered structure, several low-N configurations, $3 \le N \le 6$, expected at $h = h_{(1,0)}(N)$ are skipped. However, as can be seen from the inset in Fig. 10, for $N = 5$ and 6, the ground-state energy is smaller than the energies of these states at $h = h_{(1,0)}(N)$ only by a tiny value. For $h < 0.2$, the actual evolution of the lattice structure starts to roughly follow the London route (except for skipped state $(1,0)_6$ near $h = 0.16$) but with a small negative offset, i. e., we again see that the matching fields are systematically shifted down in comparison with their London values.

The field dependence of the energy function $G(N,q,h)$ in an extended field range is shown in Fig. 10 for the ground state and competing states. Each curve corresponds to the minimum of $G(N,q,h)$ with respect to q at fixed h and N and is marked by its value of N. We also show the first six lattice configurations that are realized with decreasing the field. The inset in the figure blows up the low-field region. We can see that many lattice configurations compete for the ground state at small fields and at several fields (e. g., at $h \approx, 0.19, 0.137, 0.105\ldots$), one or more lattice configurations have energies very close to the ground-state energy. We also note that there are several extended field ranges where in the ground state all layers are homogeneously filled with vortices ($N = 1$) even in the region of the dilute vortex lattice, e. g., $0.115 < h < 0.17$ and $0.21 < h < 0.38$.

We see that an accurate consideration within both London and Lawrence–Doniach models shows that the ground state of the Josephson vortex lattice at low temperatures does not give any preference to the lattices aligned with the layers. Therefore, for equilibrium field dependences we cannot expect to observe any strong features at the matching fields of these lattices, $B_{(1,0)}(N)$ and $B_{(1,1)}(N)$ given by Eq. (43). Nevertheless, clear commensurability oscillations have been observed experimentally in underdoped YBCO in irreversible magnetization [28, 29] and nonlinear resistivity [30]. The period of these oscillations corresponds to the fields $B_{(1,0)}(N)$, indicating that in this material, the aligned lattice $(1,0)$ occurs to be preferable for some reason. We note that in real materials, due to small differences between the energies of different configurations, aligned lattices can be selected by external factors, such as interaction with correlated disorder (twin boundaries or dislocations) or the sample surface. We also see in what follows that the aligned lattice with indices $(1,0)$ is favored by thermal fluctuations. Finally, we mention the work of Ikeda and Isotani [64], who performed similar analysis of the ground-state configurations for the field applied along the layers within the lowest Landau level approximation.

4.3. Properties of metastable states in the London model

Josephson vortices can slide easily along the layers, but there is a huge barrier for the motion across the layers. This property makes it difficult to equilibrate the lattice. It also leads to the appearance of a very large number of metastable states. The properties of these states have been considered in Refs. [57, 58]. Systematically, metastable states at a fixed c-axis period can be sampled by first slowly cooling down the superconductor at a fixed magnetic field and then in a second step decreasing the magnetic field at a low temperature [58]. We assume that the prepared starting configuration is the aligned lattice. As the c-axis period N is locked by the layers, the lattice stretches along the layers with lowering the field, i. e., the ratio $r = b/a$ decreases. During stretching, these fixed-N metastable states go through a sequence of nontrivial structural transformations. In the London regime, the aligned configuration becomes unstable at $r_0 \approx 1.51/(2\pi) \approx 0.24$ [57]. This instability is driven by the repulsion between neighboring vortices in the vertical stack. At low $r < r_0$, the pa-

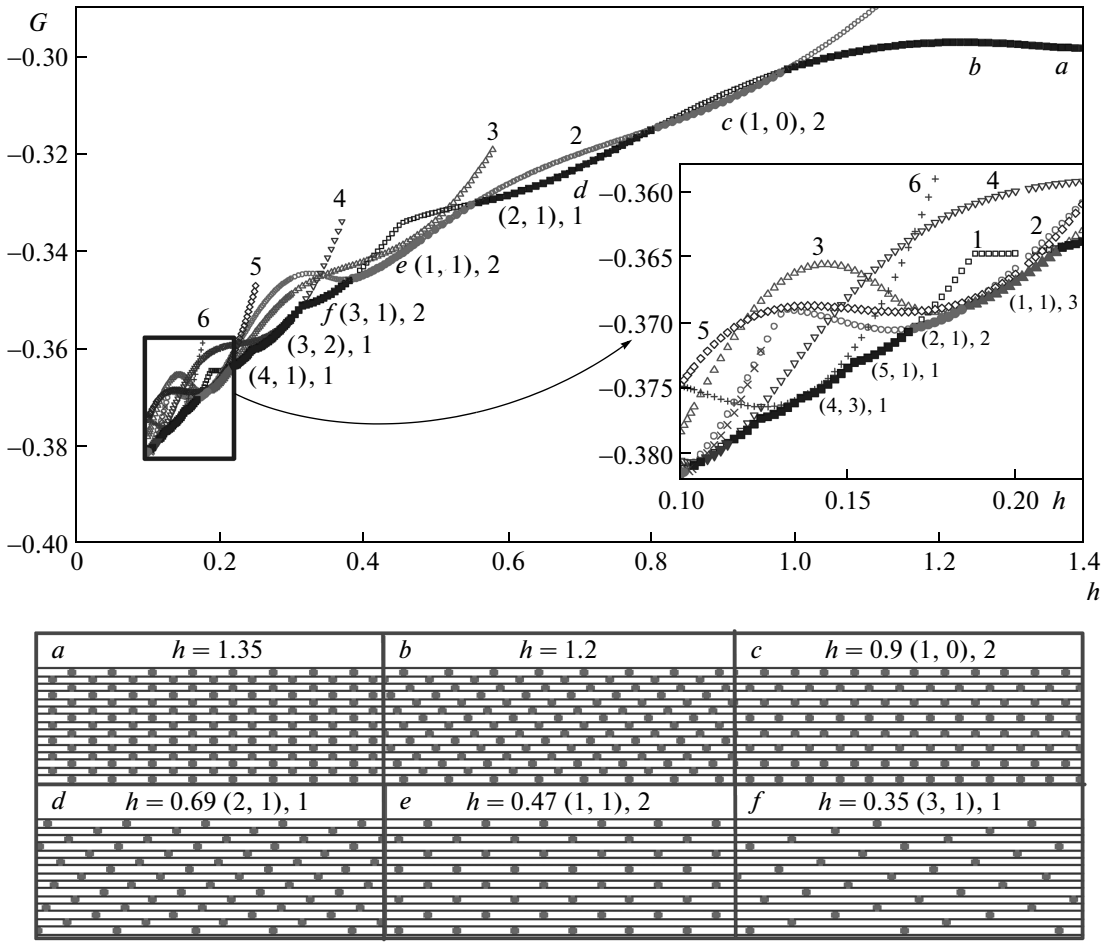

Fig. 10. Field dependence of the energy function $G(N, q, h)$ for the ground state and competing states. Each curve corresponds to the minimum of $G(N, q, h)$ with respect to q at fixed h and N. The curves are marked by the value of N. Lattice configurations in scaled coordinates are shown at six marked fields. The inset illustrates competition between different configuration at smaller fields

rameter q continuously decreases starting from $1/2$ to lower values. We found that the layeredness stabilizes the aligned structures: the critical ratio decreases to 0.231 at $N = 3$ and to 0.224 at $N = 2$. It is important to note that the shear instability occurs in the ground state only for $N = 1$ (we consider this structural phase transition in detail below). At higher values of N, this instability only occurs when the state for this given N is metastable with respect to other values of N. This instability is considered in detail below.

The statistics of metastable states has been explored in detail in Ref. [58], where the similarity to the phyllotaxis phenomenon in biological systems has been pointed out. For every r, we can find all local minima $q_i(r)$ of the energy function $G(r, q)$ with respect to q and plot all these minima in the qr plane (see Fig. 11). The obtained pattern is quite peculiar. At $r > r_0$, the only minimum is at $q_0(r) = 1/2$. Below $r = r_0$, this trajectory symmetrically splits into two. As r decreases further, many more minima appear forming a complex hierarchical structure. The pattern can be viewed as a series of "quasibifurcations" occurring near rational values of q. "Quasibifurcation" corresponds to the appearance of a new branch below a certain value of r in the vicinity of the old branch. The branches turn at the points $(q_{(m,n)}, r_{(m,n)})$ corresponding to ground states. The evolution of the initial state is described by the two main trajectories symmetrically split from $q = 1/2$. The trajectory with $q > 1/2$ "quasi-bifurcates" at $q = F_j/F_{j+1}$ where F_j are the Fibonacci numbers and approaches the "golden ratio" $(\sqrt{5} - 1)/2 \approx 0.618$ as $r \to 0$. It goes through

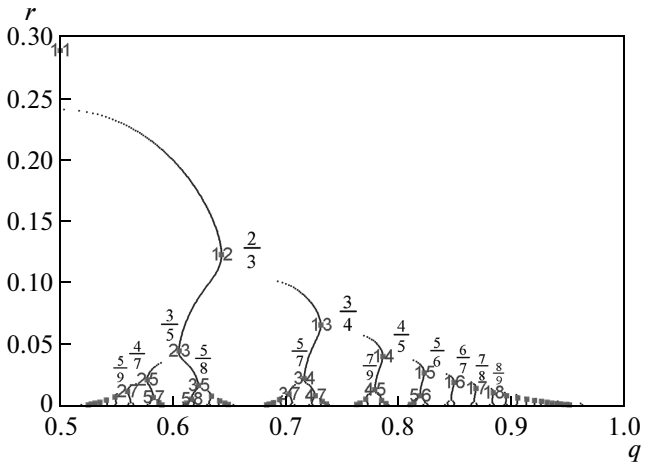

Fig. 11. Levitov's hierarchical plot of metastable states in the qr plane [58] (in this plot, q is selected within the interval $[0.5, 1]$). Each dotted curve is obtained from the local minima of the function $G_L(r, q)$ with respect to q at a fixed r. New branches appear as a result of "quasibifurcations". Each "quasibifurcation" is associated with a rational number. The branches turn at the points $(q_{(m,n)}, r_{(m,n)})$ corresponding to ground states (marked by squares and labelled by the indices mn in the plot)

ground states with the indices also described by the Fibonacci sequence, $(m, n) = (F_{j+1}, F_j)$. Unfortunately, these exciting predictions have never been verified experimentally because there is no direct way to probe the structure of the Josephson vortex lattice.

4.4. Elasticity of a dilute Josephson vortex lattice

Josephson vortices easily slide along the layers but motion across the layers is strongly suppressed by intrinsic pinning from the layers. Due to the intrinsic pinning, z-axis fluctuations of the vortex lines occur via kink formation. In moderately anisotropic layered superconductors, such as YBCO, in which the c-axis coherence length is larger than or comparable with the interlayer spacing d, the intrinsic pinning potential $V(u_z)$ can be described as a cosine function of the z-axis vortex displacements $V(u_z) = -V_0 \cos(2\pi u_z(x)/d)$. But such description becomes inadequate in strongly layered materials, where the structure of kinks is very similar to the structure of a pancake vortex.

In strongly layered materials at low temperatures, we can neglect kink formation and take only in-plane lattice deformations $u(\mathbf{r}) \equiv u_y(\mathbf{r})$ into account (planar-fluctuations model). In this case, we can derive the nonlocal elastic energy in the k-space as

$$F_{el} = \frac{1}{2}\int \frac{d^3\mathbf{k}}{(2\pi)^3} \times \\ \times \left[c_{11}(\mathbf{k})k_y^2 + c_{44}(\mathbf{k})k_x^2 + c_{66}k_z^2\right] |u(\mathbf{k})|^2 \quad (59)$$

with the elastic moduli

$$c_{66} = \frac{B_x\Phi_0}{(8\pi)^2\lambda_c^2\gamma}, \quad (60)$$

$$c_{11}(\mathbf{k}) = \frac{B_x^2/4\pi}{1+\lambda_{ab}^2k_z^2+\lambda_c^2\left(k_y^2+k_x^2\right)} - \frac{B_x\Phi_0}{(8\pi)^2\lambda_{ab}\lambda_c}, \quad (61)$$

$$c_{44}(\mathbf{k}) = \frac{B_x^2/4\pi}{1+\lambda_{ab}^2k_z^2+\lambda_c^2\left(k_y^2+k_x^2\right)} + \\ + \frac{B_x\Phi_0}{(4\pi)^2\lambda_{ab}\lambda_c}\ln\frac{1}{d\sqrt{a_z^{-2}+(\gamma k_x/\pi)^2}}. \quad (62)$$

While the tilt $[c_{44}(\mathbf{k})]$ and compression $[c_{11}(\mathbf{k})]$ moduli are not sensitive to the exact lattice structure, the formula for the shear modulus c_{66} is valid only for perfect matching between the Josephson vortex lattice and layered structure, which is achieved at matching fields (42). For a general lattice shown in Fig. 6*a* we can derive a more general expression for c_{66} using representation (48)–(49) for the lattice energy [57] and the relation between lattice deformation and change of the parameter q, $\delta q = r\,du/dz$,

$$c_{66} = \frac{B_x\Phi_0}{(8\pi)^2\lambda_c^2\gamma}g_{66}(r,q) \quad (63)$$

with

$$g_{66}(r,q) = 4r^2\frac{\partial^2}{\partial q^2}G_L(r,q) = -(4\pi)^2r^2 \times \\ \times\sum_{l=1}^{\infty}\frac{\cos(2\pi ql)\,\mathrm{ch}(2\pi rl) - \sin^2(2\pi ql) - 1}{\left(\mathrm{ch}(2\pi rl) - \cos(2\pi ql)\right)^3}l\,\mathrm{sh}(2\pi rl).$$

This formula reproduces the result in (60) for the commensurate configurations $(r, q) = (r_{(n,m)}, q_{(n,m)})$. It also describes instability of the aligned configuration $(q = 1/2)$ at $r \approx 0.24$ [57].

The softest mode in the planar model corresponds to shearing between neighboring planar arrays of Josephson vortices. The harmonic approximation breaks for this mode first. The simplest extension of the linear elastic energy that describes strong interplanar fluctuations amounts replacing the continuous displacement field $u(\mathbf{r})$ by the displacement of the planar

arrays $u_j(x,y) \equiv u(x,y,jb)$ and replacing the shear term in the energy by the nonlinear interaction term

$$\int d^3\mathbf{r}\frac{c_{66}}{2}\left(\frac{du}{dz}\right)^2 \to \\ \to \int d^2\mathbf{r}\frac{a^2c_{66}}{(2\pi)^2\,b}\sum_j\left[1-\cos\left(2\pi\frac{u_{j+1}-u_j}{a}\right)\right].$$

Such an extension has been used to study the strong-fluctuation region [65].

5. DENSE LATTICE, $B_x > \Phi_0/2\pi\gamma d^2$

The distance between Josephson vortices decreases as the magnetic field increases, and at the field $B \sim \sim B_{cr} = \Phi_0/2\pi\gamma d^2 = B_{\gamma d^2}/2\pi$ becomes of the order of the vortex-core size. In contrast to the Abrikosov vortex lattice, for which overlap of the vortex cores marks the disappearance of superconductivity, for the Josephson vortex lattice this field just marks a crossover to a new regime, the dense Josephson vortex lattice. The existence of this regime was pointed out by Bulaevskii and Clem [25]. In the dense Josephson vortex lattice, the gauge-invariant phase difference is a smoothly increasing function of distance and the Josephson coupling energy can be treated as a small perturbation. This allows for the following quantitative description.

5.1. Very high fields: Quantitative description using an expansion in the Josephson coupling

At high fields $B_x > B_{cr}$, vortices homogeneously fill all the layers. This means that all layers are equivalent and the in-plane lattice period is $\tilde{a} = 2\pi/h$ (see Fig. 12). When the strong inequality $B_x \gg B_{cr}$ ($h \gg 1$) is satisfied, Eq. (54) for the phases can be solved using an expansion with respect to the Josephson currents. In the zeroth order, we can construct a regular lattice with an arbitrary translation from layer to layer by using the form

$$\phi_n^{(0)} = \kappa\frac{n(n-1)}{2}.$$

This corresponds to the gauge-invariant phase difference

$$\varphi_{n,n+1}^{(0)} = \kappa n + h\bar{y},$$

i. e., the planar lattices in the neighboring layers are shifted by the fraction $q = \kappa/2\pi$ of the in-plane lattice spacing $\tilde{a}$. In the first order, we obtain

$$\nabla_{\bar{y}}^2\phi_n^{(1)} + \sin(\kappa n + h\bar{y}) - \sin(\kappa(n-1) + h\bar{y}) = 0$$

which gives

$$\phi_n^{(1)}(\bar{y}) = \frac{1}{h^2}\left[\sin(\kappa n + h\bar{y}) - \sin(\kappa(n-1) + h\bar{y})\right].$$

Substituting this solution in (53), we obtain the energy per unit volume up to the second order with respect to the Josephson coupling,

$$f_\phi(\kappa,h) = \frac{\varepsilon_J}{\gamma d^2}\left(1 - \frac{1-\cos\kappa}{2h^2}\right). \qquad (64)$$

We can immediately see that the minimum energy $f_{min}(h) = (\varepsilon_J/\gamma d^2)(1-1/h^2)$ is achieved at $\kappa = \pi$, corresponding to the triangular lattice shown in Fig. 12. The phase distribution in the ground state is given by

$$\phi_n(\bar{y}) \approx \pi\frac{n(n-1)}{2} + \frac{2(-1)^n}{h^2}\sin(h\bar{y}). \qquad (65)$$

From this solution, we can recover the distributions of the in-plane and Josephson currents

$$j_{y,n}(y) \approx -\frac{2(-1)^n}{h}\gamma j_J\cos\left(\frac{2\pi dB_x y}{\Phi_0}\right),$$

$$j_{z,n}(y) \approx -(-1)^n j_J \times \\ \times \sin\left[-\frac{4(-1)^n}{h^2}\sin\left(\frac{2\pi dB_x y}{\Phi_0}\right) + \frac{2\pi dB_x y}{\Phi_0}\right],$$

and a weak modulation of the in-plane field

$$B_x(y) \approx B_x - \frac{(-1)^n\Phi_0^2}{B_x(2\pi d\lambda_c)^2}\cos\left(\frac{2\pi dB_x y}{\Phi_0}\right).$$

A schematic distribution of the currents is shown in Fig. 12.

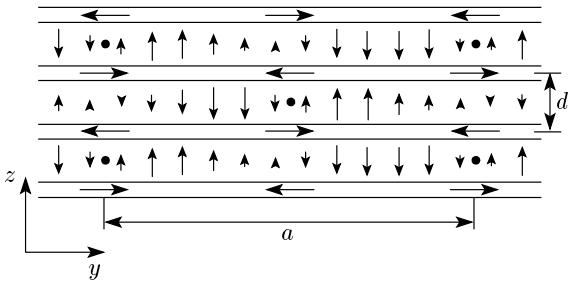

Fig. 12. Schematic distribution of currents in the dense Josephson vortex lattice. The circles mark the centers of the Josephson vortices

5.2. Dense lattice close to the crossover region. Structural phase transition

When the magnetic field approaches the crossover field $\Phi_0/(2\pi\gamma d^2)$, the perturbative approach of the previous section becomes insufficient and we have to obtain a full solution of nonlinear equation (54). The general solution for the lattice with an arbitrary phase shift κ can be written as

$$\phi_n(\bar{y}) = \kappa\frac{n(n-1)}{2} + g\left(\bar{y} + \frac{\kappa n}{h}\right), \qquad (66)$$

where $g(\bar{y})$ is a periodic function, $g\left(\bar{y} + 2\pi/h\right) = g(\bar{y})$, that obeys the equation

$$\frac{d^2g}{d\bar{y}^2} + \sin\left(g\left(\bar{y} + \frac{\kappa}{h}\right) - g\left(\bar{y}\right) + h\bar{y}\right) - \\ - \sin\left(g\left(\bar{y}\right) - g\left(\bar{y} - \frac{\kappa}{h}\right) + h\bar{y} - \kappa\right) = 0. \qquad (67)$$

The reduced energy $\bar{f} \equiv f_\phi\gamma d^2/\varepsilon_J$ can also be written in terms of $g(\bar{y})$:

$$\bar{f} = \int_0^{2\pi/h} \frac{h d\bar{y}}{2\pi}\left\{\frac{1}{2}\left(\frac{dg}{d\bar{y}}\right)^2 + \right. \\ \left. + 1 - \cos\left[g\left(\bar{y} + \frac{\kappa}{h}\right) - g\left(\bar{y}\right) + h\bar{y}\right]\right\}. \qquad (68)$$

Equation (67) does not have an analytic solution and has to be solved numerically. Lattice configurations of the dense lattice have also been investigated using the code developed for the lattice with a general period N. Both approaches give identical results. Numerical investigation shows that the triangular lattice with $\kappa = \pi$ gives the ground state for $h > 1.332$. At $h \approx 1.332$, the system has a second-order phase transition to a lower-symmetry lattice (see lattice structures for $h = 1.35$ (a) and $h = 1.2$ (b) in Fig. 10). The field dependence of κ and the corresponding lattice shift q are shown in Fig. 13. Ikeda and Isotani [64] found that within the lowest Landau level approximation, this structural phase transition occurs at a somewhat higher value, $h \approx 1.4$.

In Fig. 14, to study the validity range of the high-h approximation in the previous section, we plot the computed field dependence of the reduced energy together with its high-field asymptotics, derived in the previous section. It can be seen that the perturbative approach gives a good approximation for the energy down to $h \sim 2$.

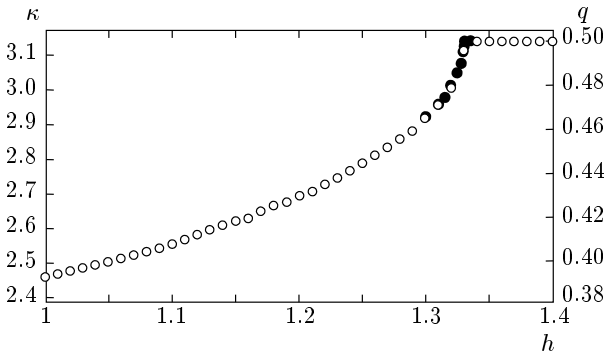

Fig. 13. Field dependence of the phase shift κ and the corresponding lattice shift q for the dense Josephson vortex lattice. At $h \approx 1.332$, the lattice experiences a continuous structural phase transition

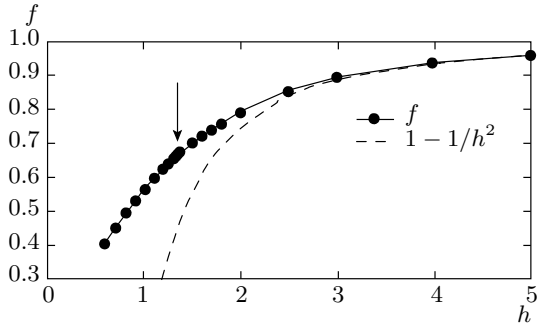

Fig. 14. Field dependence of the reduced energy for the dense Josephson vortex lattice. The dashed line shows the high-field asymptotic behavior. The arrow marks the position of the structural phase transition at $h \approx 1.332$

5.3. Elasticity of the dense lattice

In this section, we consider the deformation energy of the dense Josephson vortex lattice in the limit $h = 2\pi\gamma d^2 B_x/\Phi_0 \gg 1$. In particular, this energy serves as a starting point for the analysis of fluctuations. We follow the approach used by Korshunov and Larkin [66]. The starting point of the analysis is again the reduced LLD energy in the phase approximation (53), which we now rewrite for the general case of the phase depending on both reduced coordinates $\bar{\mathbf{r}} \equiv (\bar{x}, \bar{y}) = \mathbf{r}/\gamma d$:

$$F_\phi = E_0\sum_n \int d^2\bar{\mathbf{r}} \times \\ \times \left[\frac{1}{2}\left(\frac{d\phi_n}{d\bar{\mathbf{r}}}\right)^2 - \cos\left(\phi_{n+1} - \phi_n + h\bar{y}\right)\right]. \qquad (69)$$

The ground-state phase distribution is given by Eq. (65). We now consider small deformations of the lattice and split the total phase into a smooth part v_n and the part $\tilde{\phi}_n$ rapidly oscillating in the y direction:

$$\phi_n(\bar{\mathbf{r}}) = \pi\frac{n(n+1)}{2} + v_n(\bar{\mathbf{r}}) + \tilde{\phi}_n(\bar{\mathbf{r}}), \qquad (70)$$

where we assume that $dv_n/d\bar{y} \ll v_n$ and $\tilde{\phi}_n \ll 1$. Because the smooth part of the gauge-invariant phase difference is given by $h(\bar{y}+(v_{n+1}-v_n)/h)+\pi n$, the quantity $u_n = -(v_{n+1}-v_n)/h$ represents a local lattice displacement. Substituting representation (70) in the energy (69), expanding with respect to $\tilde{\phi}_n$, and dropping rapidly oscillating terms, we obtain

$$F_\phi \approx E_0\sum_n\int d\bar{\mathbf{r}}\left[\frac{1}{2}\left(\frac{d\tilde{\phi}_n}{d\bar{y}}\right)^2 + \frac{1}{2}\left(\frac{dv_n}{d\bar{\mathbf{r}}}\right)^2 + \right.$$
$$\left. + \left(\tilde{\phi}_{n+1}-\tilde{\phi}_n\right)\sin\left(v_{n+1}-v_n+h\bar{y}+\pi n\right)\right]. \qquad (71)$$

As $\tilde{\phi}_n$ rapidly oscillates only in y direction, we keep only its $\bar{y}$ derivative. Minimizing this energy with respect to $\tilde{\phi}_n$ gives

$$\tilde{\phi}_n \approx (-1)^n\frac{\sin\left(v_{n+1}-v_n+h\bar{y}\right)+\sin\left(v_n-v_{n-1}+h\bar{y}\right)}{h^2}.$$

Substituting this solution in Eq. (71) and averaging with respect to $\bar{y}$, we finally obtain the coarse-grained energy of the deformed dense Josephson vortex lattice [69], which we write in real units:

$$F_\phi \approx \frac{E_0}{2}\sum_n\int d\mathbf{r}\times$$
$$\times\left[\left(\frac{dv_n}{d\mathbf{r}}\right)^2 - \frac{\cos\left(v_{n-1}+v_{n+1}-2v_n\right)+1}{(\Lambda_J h)^2}\right]. \qquad (72)$$

This energy describes the phase fluctuations in a large in-plane magnetic field. The first term is just the usual in-plane phase stiffness energy. In the elasticity theory language, this term represents the compression (dv_n/dy) and tilt (dv_n/dx) contributions. The second term represents the shearing interactions between the Josephson vortex arrays in neighboring junctions. It originates from the Josephson coupling energy and can be viewed as the effective Josephson coupling renormalized by the in-plane magnetic field. Roughly, we can state that as the magnetic field increases, the effective Josephson energy decreases as $1/h^2$ and the effective Josephson length Λ_{Jh} increases linearly with h,

$$\Lambda_{Jh} = \Lambda_J h = \frac{2\pi\gamma^2 d^3 B_x}{\Phi_0}. \qquad (73)$$

For the deformation slowly changing from layer to layer, we can expand the cosine in Eq. (72) and obtain the harmonic elastic energy of the dense Josephson vortex lattice in terms of smooth phase deformations:

$$F_{\phi-el} \approx \frac{E_0}{2}\sum_n\int d\mathbf{r}\times$$
$$\times\left[\left(\frac{dv_n}{d\mathbf{r}}\right)^2 + \frac{\left(v_{n-1}+v_{n+1}-2v_n\right)^2}{2(\Lambda_J h)^2}\right] =$$
$$= \frac{E_0}{2d}\int\frac{d^2\mathbf{k}_\parallel}{(2\pi)^2}\int\limits_{-\pi/d}^{\pi/d}\frac{dk_z}{2\pi}\times$$
$$\times\left[k_\parallel^2 + \frac{2\left(1-\cos k_z d\right)^2}{(\Lambda_J h)^2}\right]|v^k|^2. \qquad (74)$$

Using the relation between the phase perturbation and lattice displacements

$$v^k = -\frac{hu^k}{\Lambda_J\left(\exp(ik_z d)-1\right)}, \qquad (75)$$

we can rewrite the elastic energy in a more traditional way, via lattice deformations

$$F_{\phi-el} = \frac{1}{2}\int\frac{d^2\mathbf{k}_\parallel}{(2\pi)^2}\int\limits_{-\pi/d}^{\pi/d}\frac{dk_z}{2\pi}\times$$
$$\times\left[c_{11}(k_z)k_\parallel^2 + c_{66}\tilde{k}_z^2\right]|u^k|^2 \qquad (76)$$

with the elastic constants

$$c_{11}(k_z) = \frac{B_x^2}{4\pi}\frac{1}{\tilde{k}_z^2\lambda_{ab}^2}, \quad c_{66} = \frac{\Phi_0^2}{32\pi^3 d^2\gamma^4\lambda_{ab}^2},$$

where we use the notation $\tilde{k}_z \equiv 2\sin\left(k_z d/2\right)/d$. We note that in our case, the nonlocal tilt modulus $c_{44}(k_z)$ is identical to the compression modulus $c_{11}(k_z)$ and they coincide with elastic moduli within the anisotropic London model (61) and (62) in the limit $\tilde{k}_z\lambda_{ab} \gg \gg 1, k_x\lambda_c$. These elastic energies (74) and (76) can be used to study weak fluctuations and weak pinning of the dense Josephson vortex lattice. The shear modulus is field independent in the dense-lattice regime. It can be verified to match the dilute-lattice result (60) at the crossover field.

5.4. Lattice configurations and magnetic oscillations in finite-size samples

In this section, we consider dense-lattice configurations in finite-size samples. This study is actually

motivated by experimental observations of magnetic oscillations in small-size BSCCO mesas with lateral sizes 2–20 μm [44–48]. Such small-size mesas behave as stacks of intrinsic Josephson junctions with strong inductive coupling between the neighboring junctions. The detailed analytic theory describing the magnetic field dependences of lattice configurations and the critical current has been developed in Ref. [67]. Lattice structures also have been extensively explored numerically in [45, 47, 68, 69], and both approaches give identical results. In a small-size sample, the lattice structure is determined by two competing interactions: the interaction with boundaries, which favors an aligned rectangular configuration, and the bulk shearing interaction between neighboring layers, which favors a triangular configuration. Depending on the mesa width L and the magnetic field, two very different regimes can be realized. In the large-size regime, the vortex lattice is triangular and is only deformed near the edges. In the small-size regime, the lattice structure experiences a periodic series of phase transitions between rectangular and triangular configurations. The triangular configurations in this regime are realized only in narrow regions near magnetic field values corresponding to an integer number of flux quanta per junction where the interaction with edges vanishes. The typical width of the mesa that separates these two regimes is given by the length Λ_{Jh} in Eq. (73), which is proportional to the applied magnetic field. Hence, the crossover from one regime to another is driven by the magnetic field and the corresponding crossover field scale is $B_L = B_{cr}L/\Lambda_J = L\Phi_0/(2\pi\gamma^2 d^3)$; for $B_x > B_L$ the small-size regime is realized. The size–field phase diagram is shown in Fig. 15. The regimes are characterized by distinctly different oscillating behavior of the critical current as a function of the magnetic field. In the small-size regime, the critical current oscillates with the period of one flux quantum per junction, similar to a single junction. In the large-size regime, due to the triangular lattice ground state, the oscillation period is half the flux quantum per junction.

The quantitative study of the described behavior is based on reduced energy (69), which has to be rewritten for the finite-size case $0 < \bar{y} < \bar{L} \equiv \bar{L}_y$ and also assuming that the system is uniform along the field direction, i. e., $\int d\bar{\mathbf{r}} \to \bar{L}_x \int_0^{\bar{L}} d\bar{y}$. This energy has to be supplemented with the boundary conditions at the edges, $d\phi_n/d\bar{y} = 0$ for $\bar{y} = 0, \bar{L}$. The important parameter in the case of a finite-size sample is the total magnetic flux through one junction, $\Phi = B_x dL$, which is connected with the reduced magnetic field by the relation $h\bar{L} = 2\pi\Phi/\Phi_0$. In the dense-lattice limit, we again use the representation in Eq. (70) containing the smooth phase v_n, and the rapidly oscillating component $\tilde{\phi}_n$. It is natural to assume that the interactions with the boundaries preserve the alternating nature of the vortex lattice. In this case, symmetry allows taking the smooth phase in the form

$$v_n(\bar{y}) = \alpha n + (-1)^n v(\bar{y}), \tag{77}$$

where α describes the translational displacement of the lattice and v describes lattice deformations with respect to the triangular lattice. In particular, it can be shown that the maximum value of $v(\bar{y})$, $v_{max} = \pi/4$, describes the rectangular lattice, i. e., identical ϕ_n in all layers up to a 2π phase shift. The rapid phase corresponding to the smooth phase (77) becomes $\tilde{\phi}_n(\bar{y}) \approx \approx (-1)^n 2\cos(2v)\sin(\alpha + h\bar{y})/h^2$. Averaging with respect to the rapid oscillations for such $v_n(\bar{y})$ gives the reduced energy $f_\phi = F_\phi \Lambda_J/(NL_x E_0)$ per layer and per unit length along x:

$$f_\phi \approx -\frac{1}{h}\left[\sin(2v_0)\cos\alpha - \sin(2v_L)\cos\left(h\bar{L}+\alpha\right)\right] + \\ + \frac{1}{2}\int_0^{\bar{L}} d\bar{y}\left[\left(\frac{dv}{d\bar{y}}\right)^2 - \frac{1+\cos(4v)}{h^2}\right], \tag{78}$$

where the bulk part directly follows from Eq. (72) for general $v_n(\bar{y})$. Varying this energy with respect to $v(\bar{y})$, we obtain that it obeys the static sine-Gordon equation

$$\frac{d^2 v}{d\bar{y}^2} - \frac{2}{h^2}\sin(4v) = 0 \tag{79}$$

with the boundary conditions

$$\frac{dv}{d\bar{y}}(0) = -\frac{2}{h}\cos(2v_0)\cos\alpha, \\ \frac{dv}{d\bar{y}}(L) = -\frac{2}{h}\cos(2v_L)\cos\left(h\bar{L}+\alpha\right). \tag{80}$$

Substituting the solution of these equations in energy functional (78) gives the energy as a function of the lattice shift α, $f_\phi(\alpha)$. The minimum of the energy with respect to α gives the ground state for given h and $\bar{L}$. Higher-energy states at other values of α typically carry a finite current. The total Josephson current flowing through the stack is proportional to $df_\phi/d\alpha$. Taking derivative of functional (72) with respect to α and assuming that at every α it is minimized with respect to $v(u)$, we obtain the total current in units of $j_J \Lambda_J L_x$:

$$J(\alpha) = \frac{1}{h} \times \\ \times \left[\sin(2v_0)\sin\alpha - \sin(2v_L)\sin\left(h\bar{L}+\alpha\right)\right]. \tag{81}$$

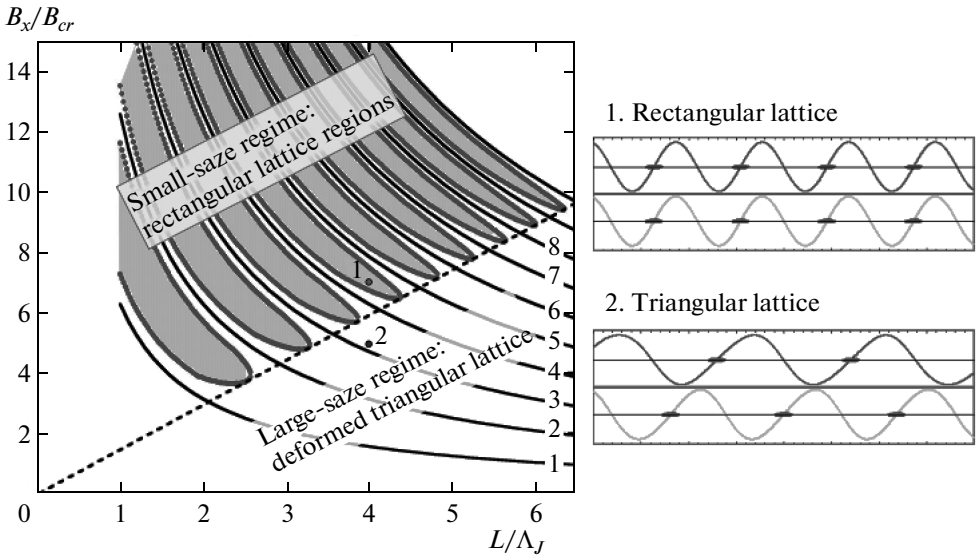

Fig. 15. Size–magnetic field phase diagram of the confined Josephson-junction stack. The dashed line separates the large-size and small-size regimes. Black lines correspond to integer flux quanta per junction. Shaded areas mark regions of the rectangular-lattice ground state. Representative lattice configurations in two points are illustrated by plots of oscillating Josephson currents in two neighboring layers. Small ellipses mark the centers of the Josephson vortices

An important consequence of this equation is that a nonzero current exists only if the surface deformations v_0 and v_L are finite.

The general solution of Eqs. (79) and (80) can be written in terms of the elliptic integrals, and an elaborate analytic analysis is possible [67]. Here, we summarize the most important results of this analysis for two limit cases.

In the large-size regime, $L \gg \Lambda_{Jh}$ or $B_x \ll B_L$, the smooth alternating deformation $v(\bar{y})$ has a solution in the form of two isolated surface solitons [67]. For example, near the edge $\bar{y} = 0$, such a soliton solution decaying from the surface into the balk is given by the well-known formula for the sine-Gordon kink

$$\operatorname{tg} v = \operatorname{tg} v_0 \exp\left(-2\sqrt{2}\bar{y}/h\right), \qquad (82)$$

where the boundary value v_0 can be found from the boundary condition (80), leading to $\operatorname{tg}(2v_0) = \sqrt{2}\cos\alpha$. Using this solution, we can find the surface energy and surface current for the edge $\bar{y} = 0$ as functions of the lattice displacement α:

$$f_s(\alpha) = \frac{1}{\sqrt{2}h}\left(1 - \sqrt{2 + \cos 2\alpha}\right), \qquad (83)$$

$$j_s(\alpha) = -\frac{1}{\sqrt{2}h}\,\frac{\sin 2\alpha}{\sqrt{2 + \cos 2\alpha}}. \qquad (84)$$

The 2α periodicity of these results is a consequence of the triangular lattice structure: the change of α by π corresponds to the vertical lattice displacement by one layer. A similar solution is realized at the opposite edge $\bar{y} = \bar{L}$. Its energy and current can be obtained from the above results using the substitution $\alpha \to \alpha + h\bar{L}$. For a wide stack, we can neglect the interaction between the solitons, and the total Josephson current is then given by the sum of two independent surface currents,

$$J(\alpha) = j_s(\alpha) + j_s(\alpha + h\bar{L}).$$

The critical current J_c can be found as a maximum of $J(\alpha)$ with respect to α, which gives the following result in real units:

$$J_c(B) = J_J \frac{\Phi_0}{2\pi dLB_x}\mathcal{F}\left(\frac{2\pi dLB_x}{\Phi_0}\right), \qquad (85)$$

where $J_J = j_J L L_x$ is the maximum Josephson current through the sample at zero field, and the oscillating function $\mathcal{F}(\chi)$ has the period π and in the range $0 < \chi < \pi/2$ can be approximated by $\mathcal{F}(\chi) \approx \approx 0.128 + 0.888\cos(\chi) + 0.021\cos(3\chi)$. We can see that in this regime, the product $B_x J_c$ has the periodicity of half the flux quantum per junction and reaches maxima at the points $\Phi = dLB_x = j\Phi_0/2$ with $B_x J_{c,max} \approx \approx 1.035 J_J \Phi_0/(2\pi dL)$. This corresponds to the low-field part of the plot in Fig. 16. All other properties of the sample should also oscillate with the period of half the flux quantum. Such oscillations of the flux-flow resistivity in BSCCO micro-mesas were first detected

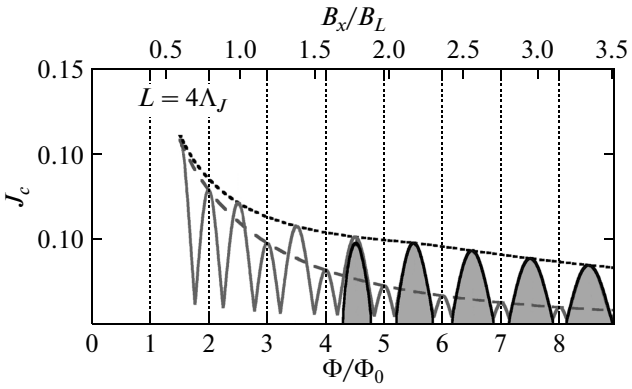

Fig. 16. Illustration of the oscillating magnetic field dependence of the critical current for $L = 4\Lambda_J$. Crossover between the $\Phi_0/2$ and Φ_0 periodicities is seen at $h\bar{L} = B_x/B_L \sim 1$. Shaded areas show the regions of stable rectangular lattice

experimentally in Ref. [44] and later confirmed by several experimental groups.

In the small-size regime $L < \Lambda_{Jh}$ or $B_x > B_L$, the interaction with edges dominates. As a consequence, extended regions of the rectangular lattice appear in the phase diagram (see Fig. 15). The energy of the rectangular lattice, $v = \pm\pi/4$, coincides with the well-known result for a single junction

$$f_{rect}(\alpha) = -\frac{2}{h}\sin\left(\frac{hL}{2}\right)\sin\left(\alpha + \frac{hL}{2}\right) \qquad (86)$$

and has the minimum $f_{rect} = -2\left|\sin\left(hL/2\right)\right|/h$ at $\alpha = -hL/2 + \delta\pi/2$ with $\delta = \mathrm{sign}\left[\sin\left(hL/2\right)\right]$. An accurate analysis [67] shows that the rectangular lattice is stable with respect to small deformations at $\alpha = -h\bar{L}/2 + \pi/2$ in the regions $|h\bar{L}/2\pi - (k+1/2)| < 1/4$ only if the inequality

$$\left|\sin\left(h\bar{L}/2\right)\right| < \mathrm{tg}\left(\sqrt{2}\bar{L}/h\right)/\sqrt{2} \qquad (87)$$

is satisfied. These regions are plotted in the phase diagram in Fig. 15. This means that the rectangular lattices first appear in the ground state at the points $h\bar{L} = (k+1/2)2\pi$ for $\bar{L}/h \le l_1 = \arctan\left(\sqrt{2}\right)/\sqrt{2} \approx \approx 0.675$. This corresponds to the dashed line shown in the phase diagram in Fig. 15. But if L/h is only slightly smaller than this value, the rectangular lattice becomes unstable as the current increases and the configuration at the critical current still corresponds to the deformed lattice. The accurate analysis shows that there is another typical value of the ratio L/h, $L/h = l_2 \approx 0.484$, below which the rectangular lattice remains stable up to the critical current.

In the region $h \gg \bar{L}$, the rectangular lattice is realized in the most part of the phase diagram except narrow regions in the vicinity of the integer-flux quanta lines $h\bar{L}/2\pi = \Phi/\Phi_0 = k$, where the interaction with the edges vanishes. Switching between the rectangular and triangular lattices in the ground state occurs via a first-order phase transition [67] at the transition fields determined by the equation

$$\left|\sin\left(\frac{h_t\bar{L}}{2}\right)\right| = \frac{3}{2}\frac{\bar{L}}{h_t}. \qquad (88)$$

At high fields, the critical current approaches the classical Fraunhofer dependence for a single small junction, $J_F(\Phi) = J_J|\sin(\pi\Phi/\Phi_0)|/|\pi\Phi/\Phi_0|$. Two important deviations persist at all fields and sizes: (i) Near the points $\Phi = k\Phi_0$, due the phase transitions to the triangular lattice, the critical current never drops to zero and actually always has small local maxima; (ii) Away from the points $\Phi = k\Phi_0$, the critical current is reached at the instability point of the rectangular vortex lattice and it is always somewhat smaller than the "Fraunhofer" value $J_F(\Phi)$.

In the region $B \sim B_L$, the crossover between the two described regimes takes place. In the oscillations of the critical current, this crossover manifests itself by breaking the $\Phi_0/2$ periodicity: the maxima at the half-integer flux-quantum points $\Phi = (k+1/2)\Phi_0$ progressively become larger while the maxima at the integer flux-quantum points $\Phi = k\Phi_0$ become smaller. This crossover behavior of the critical current is illustrated in Fig. 16. Such behavior was indeed observed experimentally in very narrow BSCCO mesas [45, 47, 48].

6. THERMAL FLUCTUATIONS

In this section, we consider thermal fluctuations effects for the Josephson vortex lattice. Confinement of the vortex cores in between the layers leads to strong suppression of the vortex motion across the layers, which can only occur via formation of kinks. Therefore, as a first step, we can neglect these energy-costly displacements and consider only planar fluctuations of vortices along the layers. This simple model describes fluctuation behavior in the most part of the field–temperature phase diagram, but it occurs to be insufficient for describing the melting transition of the lattice. In general, thermal effects for Josephson vortices are much weaker than for a pancake-vortex lattice, and phase transformations are expected only in the vicinity of the transition temperature. On the other

hand, due to the intrinsic pinning potential and involvement of kink excitations, the overall behavior near the melting line is rather complicated and, in spite of quite extensive theoretical effort [65, 66, 70–74] and numerical simulations [75, 76], there is no clear consensus on the nature of the melting transition and structure of the phase diagram for the magnetic field aligned with the direction of the layers.

6.1. Thermal effects for the dilute Josephson vortex lattice: the intermediate phase problem

A standard first step to study thermal fluctuation effects is to evaluate the mean-squared local fluctuation displacement from elastic energy (59)[4]:

$$\langle u^2 \rangle = \int \frac{d^3\mathbf{k}}{(2\pi)^3} \frac{T}{c_{11}(\mathbf{k})k_y^2 + c_{44}(\mathbf{k})k_x^2 + c_{66}k_z^2}. \quad (89)$$

Introducing the reduced wave vector $\tilde{\mathbf{k}}$ as

$$k_x = k_{BZ}\tilde{k}_x/\sqrt{\gamma}, \quad k_y = k_{BZ}\tilde{k}_y/\sqrt{\gamma}, \quad k_z = k_{BZ}\sqrt{\gamma}\tilde{k}_z, \quad (90)$$

where $k_{BZ} = \sqrt{4\pi B_x/\Phi_0}$ is the average wave vector of the Brillouin zone, we rewrite this integral in a more explicit form

$$\langle u^2 \rangle = \frac{(4\pi)^2 k_{BZ}\lambda_c^2 T}{\sqrt{\gamma}\Phi_0 B_x} \int \frac{d^3\tilde{\mathbf{k}}}{(2\pi)^3} \left[\left(\frac{1}{\tilde{k}^2} - \frac{1}{4} \right) \tilde{k}_y^2 + \left(\frac{1}{\tilde{k}^2} + \ln \frac{b_0/d}{\sqrt{1+\beta^2\tilde{k}_x^2}} \right) \tilde{k}_x^2 + \frac{\tilde{k}_z^2}{4} \right]^{-1}$$

with $\beta \sim 1$. Evaluating this integral yields

$$\frac{\langle u^2 \rangle}{a_0^2} = \frac{0.12T}{b_0\sqrt{\ln(b_0/d)\varepsilon_0}}, \quad (91)$$

where $a_0 = \sqrt{\gamma\Phi_0/B_x}$ and $b_0 = \sqrt{\Phi_0/\gamma B_x}$ are the typical lattice constant in the y and z directions. From this result, we can obtain an estimate for the typical temperature at which fluctuations become strong [65]:

$$T_f \sim b_0\sqrt{\ln(b_0/d)\varepsilon_0(T_f)}. \quad (92)$$

Unfortunately, this temperature is located very close to T_c, where we cannot use the approximations underlying Eq. (59), e. g., neglect thermal activation of kinks and antikinks. We can conclude that the model of planar fluctuations given by elastic energy (59) is not sufficient to describe the melting of the Josephson vortex lattice [65]. The temperature scale in (92) is much higher than the corresponding temperature scale for the pancake vortex lattice [19], meaning that thermal-fluctuation effects for the Josephson vortex lattice are much weaker than for the pancake vortex lattice.

We can estimate the typical temperature above which kink formation strongly influences the fluctuation displacements of the vortex lines. In an isolated line, the typical distance between thermally excited kinks is given by

$$L_{kink} = \xi_{kink}\exp(E_{kink}/T), \quad (93)$$

where $E_{kink} \approx d\varepsilon_0\ln(\gamma d/\xi_{ab})$ is the kink energy. Usually, it is assumed that the preexponential factor ξ_{kink} is of the order of the in-plane coherence length ξ_{ab} [72]. Analysis of fluctuations of the order parameter near the core [77] gives a somewhat more accurate estimate $\xi_{kink} \sim \xi_{ab}\sqrt{T/d\varepsilon_0}$. Typical k_x contributing to fluctuation displacement (89) can be estimated as $k_x \sim \pi/b_0$. Therefore, the kinks start to contribute to thermal wandering if $L_{kink} < b_0$. This gives an estimate for the typical temperature

$$T_{kink} = E_{kink}/\ln(b_0/\xi_{kink}). \quad (94)$$

In the limit $\gamma > \xi_{ab}/d$, we obtain

$$T_{kink} = d\varepsilon_0(T_{kink})\frac{\ln(\gamma d/\xi_{ab})}{\ln(b_0/\xi_{kink})}. \quad (95)$$

It follows that even though this temperature is smaller then T_f in (92), it is also located close to the fluctuation region near T_c and very slowly decreases with increasing the magnetic field.

The model of planar fluctuation belongs to the universality class of the three-dimensional XY model, and hence the phase transition described by this model has to be continuous. In spite of the insufficiency of this model, this suggests that the melting transition for the magnetic field applied along the layers may become continuous for sufficiently high anisotropy. It was indeed observed experimentally in [78] and in [30] that the melting transition in YBCO becomes continuous when the magnetic field is aligned with the layers. Continuous melting of the Josephson vortex lattice also has been observed in numerical simulations in [75]. The simulation parameters in this work, however, correspond to the regime of dense lattice, which is considered below.

[4] As in most theoretical papers, the temperature is measured in energy units.

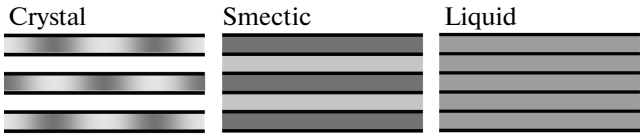

Fig. 17. Possible phases for the field applied along the layers. Grey level illustrates the average vortex density. In the intermediate smectic phase suggested in Ref. [72], density is modulated only in the direction perpendicular to the layers

A description of the fluctuating Josephson vortices taking kink–antikink formation into account is much more complicated problem and possibilities for analytic progress are quite limited. General scenarios of Josephson-vortex-lattice melting have been discussed in [72]. It was argued there that an aligned lattice may melt via an intermediate smectic phase, in which the average vortex density is modulated only in the direction perpendicular to the layers but no order is preserved in the direction of the layers, as illustrated in Fig. 17. The density modulation period has to be equal to the integer number of layers. The developed Landau theory of the liquid-to-smectic transition suggests that this transition has to be of the second order. Static and dynamic properties of the intermediate smectic phase have been described in detail. In particular, it was argued in [75] that this phase is characterized by a finite but very large tilt modulus, corresponding to a very small transversal susceptibility $\mu_z = B_z/H_z$, and by very small in-plane resistivity. Both these properties appear due to the thermally activated "superkink" excitations, in which one vortex is moved across the layers by one smectic period. While the density modulation remains static and oriented parallel to the layers, these excitations may facilitate tilting of the magnetic induction with respect to the layers and flux motion in the z-axis direction. In spite of its physical appeal, the theory in [72] is not quantitative. It does not predict locations of the transitions in the field–temperature plane, their thermodynamic signatures, and the width of the intermediate-phase region. The very existence of the intermediate smectic phase has been not rigorously proven. Alternatively, the crystal may melt directly into the liquid via a first-order phase transition.

A more quantitative study based on the density-functional theory was performed in [74]. The intrinsic pinning potential in this study was modeled by the cosine function and its strength was used as an adjusting parameter. It was found that the smectic phase exists for a sufficiently strong periodic potential only for one type of aligned lattice, which in our notation corresponds to $(m, n) = (1, 0)$, and with one empty layer between the layers filled with Josephson vortices, i. e., with $N = 2$. According to the analysis in Sec. 4.2, such a lattice is realized in the ground state within the field interval $[0.8 - 0.98]\Phi_0/(2\pi\gamma d^2)$. The melting scenario via the intermediate smectic phase is most probable in this field range.

6.2. Elimination of the lattice rotational degeneracy by thermal fluctuations

The dilute lattice at small fields is approximately degenerate with respect to elliptic rotations, as was discussed in Sec. 4. This degeneracy is partially eliminated by the intrinsic pinning potential and by the corrections to the intervortex interactions due to the discreteness of the layered structure. The latter effect becomes noticeable only at high magnetic fields approaching the crossover field. Because the Josephson vortices mainly fluctuate along the layer direction, the fluctuation correction to the free energy depends on the lattice orientation with respect to the layers and also eliminates the elliptic degeneracy. Therefore, the Josephson vortex lattice at small fields gives a physical realization of a system in which the ground state is highly degenerate at zero temperature and this degeneracy is eliminated by thermal fluctuations. Similar behavior is realized in some frustrated magnetics and is known as "order as an effect of disorder" [79]. As a natural way to prepare the ground state is to cool system in fixed field, it is important to understand how the ground-state configuration evolves with the temperature.

In this section, we consider the orientation-dependent entropy correction to the free energy. This allows us to trace evolution of the ground-state configurations with increasing field at finite temperature. Qualitatively, fluctuations favor soft lattices, with smaller elastic constants. We can then expect that the entropy correction favors the aligned lattice $(1, 0)$, because for this lattice the shear deformations occur along the closed-packed direction.

The orientation-dependent entropy correction is determined by the short-wavelength lattice deformations, and the long-wavelength elastic approximation in the previous section is not sufficient. The elastic energy for planar deformations in the whole Brillouin zone is given by

$$F_{el} = \int \frac{d^3\mathbf{k}}{(2\pi)^3} \frac{\Phi_{JVL}(\mathbf{k})}{2} |u(\mathbf{k})|^2 \qquad (96)$$

with

$$\Phi_{JVL}(\mathbf{k}) = \frac{B_x^2}{4\pi} \times$$
$$\times \sum_{\mathbf{Q}} \left(\frac{(k_y - Q_y)^2 + k_x^2}{1+\lambda_{ab}^2(k_z-Q_z)^2+\lambda_c^2(k_y-Q_y)^2 + \lambda_c^2 k_x^2} - \right.$$
$$\left. - \frac{Q_y^2}{1 + \lambda_{ab}^2 Q_z^2 + \lambda_c^2 Q_y^2} \right), \quad (97)$$

where $\mathbf{Q} = (Q_y, Q_z)$ are the reciprocal-lattice vectors. The fluctuation correction to the free energy is given by

$$\delta f_T = -\frac{T}{2} \int\limits_{-\infty}^{\infty} \frac{dk_x}{2\pi} \int\limits_{BZ} \frac{dk_y dk_z}{(2\pi)^2} \ln \frac{C}{\Phi_{JVL}(\mathbf{k})}. \quad (98)$$

Calculation of this correction is described in detail in Appendix C. Combining the result of this calculation with the London-limit presentation of the lattice interaction energy (48), we represent the orientation-dependent part of the total free energy at finite temperature in the form

$$\delta f_a = \frac{B_x}{\Phi_0} \frac{\varepsilon_0}{\gamma} \left(G_L - \frac{T}{\varepsilon_0} \sqrt{\frac{\gamma B_x}{\pi \Phi_0}} g_a \right). \quad (99)$$

The numerically computed orientation-dependent correction $g_a(\theta, h)$ in the range $0.001 < h < 0.1$ is well described by

$$g_a(\theta, h) \approx g_6(h) \cos(6\theta)$$
$$\text{with} \quad (100)$$
$$g_6(h) \approx \frac{0.01}{\sqrt{\ln(514/h)}}.$$

The fluctuations give the largest negative contribution at $\theta = 0$, meaning that they indeed favor the aligned lattice (1,0).

We compare the orientation-dependent entropy correction with the correction due to the layered structure considered in Sec. 4.2. We can see that these corrections compete: the first one favors the $(1, 0)$ orientation while the second one favors the (1,1) orientation. The entropy correction decays with decreasing fields as $\sqrt{B_x}$ and at small fields always exceeds the "layeredness" correction, which decays as B_x^2. We estimate that the "layeredness" correction exceeds the fluctuation correction when B_x exceeds the temperature-dependent field scale

$$B_{x,T} = \frac{\Phi_0}{2\pi\gamma d^2} \left[\frac{T/d\varepsilon_0}{\sqrt{\ln(C_T d\varepsilon_0/T)}} \right]^{2/3}$$

with $C_T \approx 2.6 \cdot 10^4$.

6.3. Fluctuations and melting of the dense Josephson vortex lattice

Using elastic energy (74), we can evaluate the mean-squared fluctuation of the in-plane phase

$$\left\langle \phi_n^2 \right\rangle \approx \left\langle v_n^2 \right\rangle = \frac{dT}{E_0} \int \frac{d^2\mathbf{k}_\parallel}{(2\pi)^2} \int\limits_{-\pi/d}^{\pi/d} \frac{dk_z}{2\pi} \frac{1}{k_\parallel^2 + \frac{8}{(\Lambda_J h)^2} s_z^4}$$

with $s_z(k_z) = \sin(k_z d/2)$ and the lattice displacement $u_n = -\Lambda_J \left(v_{n+1} - v_n \right)/h$:

$$\left\langle u^2 \right\rangle = \frac{dT\Lambda_J^2}{E_0} \int \frac{d^2\mathbf{k}_\parallel}{(2\pi)^2} \int\limits_{-\pi/d}^{\pi/d} \frac{dk_z}{2\pi} \frac{4 s_z^2}{k_\parallel^2 + \frac{8}{(\Lambda_J h)^2} s_z^4}.$$

Renormalization of the effective coupling is determined by the average

$$\left\langle (v_{n-1} + v_{n+1} - 2v_n)^2 \right\rangle =$$
$$= \frac{dT}{E_0} \int \frac{d^2\mathbf{k}_\parallel}{(2\pi)^2} \int\limits_{-\pi/d}^{\pi/d} \frac{dk_z}{2\pi} \frac{16 s_z^4}{k_\parallel^2 + \frac{8}{(\Lambda_J h)^2} s_z^4}.$$

All above integrals diverge logarithmically at large $k_\parallel$. This divergence has to be cut off at $k_\parallel \sim 1/\xi_{ab}$. As usual for quasi-two-dimensional systems, the weak interlayer coupling cuts off the logarithmic divergence at small $k_\parallel$. Evaluating the integrals, we obtain

$$\left\langle \phi_n^2 \right\rangle \approx \frac{T}{2\pi E_0} \ln \left(\frac{\Lambda_J h}{\xi_{ab}} \right), \quad \left\langle u^2 \right\rangle \approx \frac{T\Lambda_J^2}{\pi h^2 E_0} \ln \left(\frac{\Lambda_J h}{\xi_{ab}} \right),$$

$$\left\langle (v_{n-1} + v_{n+1} - 2v_n)^2 \right\rangle \approx 6 \left\langle \phi_n^2 \right\rangle \approx \frac{3T}{\pi E_0} \ln \left(\frac{\Lambda_J h}{\xi_{ab}} \right).$$

Fluctuations become strong and the harmonic approximation breaks down when $\left\langle (v_{n-1} + v_{n+1} - 2v_n)^2 \right\rangle \sim$ ~ 1, corresponding to $\left\langle \phi_n^2 \right\rangle \sim 1/6$ and $\left\langle u^2 \right\rangle \sim a^2/3$ with $a = \Lambda_J/h$ being the in-plane lattice constant. This gives the temperature scale

$$T_f = \frac{E_0(T_f)}{\ln(\Lambda_J h/\xi_{ab})} = \frac{\varepsilon_0(T_f) d}{\pi \ln(\Lambda_J h/\xi_{ab})}. \quad (101)$$

As $E_0(0) \gg T_c$ (typically, for BSCCO, $E_0(0) \sim$ ~ 250–$300K$), this temperature scale usually corresponds to temperatures close to T_c. It is somewhat lower than the corresponding temperature scale (92) for the dilute lattice and even smaller than temperature scale (95) for kink formation in the dilute lattice.

We next discuss the melting transition of the dense lattice based on the energy (72) describing weakly coupled two-dimensional systems. Behavior of such a system has to be similar to that of the layered XY model [80] and a layered superconductor in zero magnetic field [81]. In the ordered phase of such systems, below the Berezinskii–Kosterlitz–Thouless temperature for a single layer, a weak interlayer coupling is always relevant, cannot be treated as a small perturbation, and restores three-dimensional long-range order. The transition in such systems is expected to be continuous and to occur slightly above the Berezinskii–Kosterlitz–Thouless transition of an isolated layer that occurs at the temperature $T_{KT} = \pi E_0(T_{KT})/2$. This is in spite of the fact that the interplane fluctuations actually become strong at the temperature (101), which is significantly smaller than the transition temperature T_{KT} in an isolated layer.

The melting transition of the dense lattice was studied numerically in [75] using the frustrated XY model. The authors claimed that the melting transition is continuous at high field and changes to a first-order transitions when the field drops below $B = \Phi_0/2\sqrt{3}\gamma d^2 \approx 1.8\Phi_0/2\pi\gamma d^2$. It is not clear how universal this field is. In principle, it may be sensitive to the kink energy, which depends on the ratio $\gamma d/\xi_{ab}$.

Experimentally, an indication of the melting transition in the dense-lattice regime was found in small-size BSCCO mesas in [46], where the temperature dependence of magnetic oscillations discussed in Sec. 5.4 was explored. It was found that in the field range 0.6–0.8 tesla, the magnetic oscillations of the flux-flow voltage rapidly decrease with increasing temperature and are completely suppressed by thermal fluctuations at temperatures ~ 4 K below the transition temperature.

7. SUMMARY

In this review, we considered in detail the static properties of the Josephson vortex lattice following from the Lawrence–Doniach model in the London approximation, which mostly describes properties of superconductors in terms of the distribution of the order-parameter phase. We reviewed the properties of an isolated vortex as well as the structure and energetics of the vortex lattice in both dilute and dense regimes. In addition to standard properties, our consideration includes quite subtle nontrivial effects, such as the influence of thermal fluctuations on the orientation of the vortex lattice. We did not touch on dynamic properties of the lattice, which have became a separate large field.

A. E. K would like to thank L. N. Bulaevskii, M. Tachiki, and X. Hu for many useful discussions of theoretical issues and Yu. I. Latyshev, I. Kakeya, T. Hatano, S. Bending, V. K. Vlasko-Vlasov, A. Tonomura, and A. A. Zhukov for the discussions of relevant experimental data. A. E. K. is supported by UChicago Argonne, LLC, operator of Argonne National Laboratory, a U.S. Department of Energy Office of Science laboratory, operated under contract № DE-AC02-06CH11357.

APPENDIX A

Calculation of the nonlocal line-tension energy of a single line

For deformations with wave vectors $|k_x| \gg 1/\lambda_c$, screening effects can be neglected and the energy variation is determined by the phase part of energy, which we write using scaled in-plane coordinates $(\bar{x}, \bar{y}) = (x/\gamma d, y/\gamma d)$ as

$$\delta F \approx E_0 \sum_n \int d\bar{x} \int d\bar{y} \times \\ \times \left[\frac{1}{2}\left(\nabla_\parallel \phi_n\right)^2 - \cos\left(\phi_{n+1} - \phi_n\right) - \right. \\ \left. - \frac{1}{2}\left(\nabla_{\bar{y}} \phi_n^{(0)}\right)^2 + \cos\left(\phi_{n+1}^{(0)} - \phi_n^{(0)}\right)\right], \quad \text{(A.1)}$$

where $\phi_n^{(0)}(\bar{y})$ is the straight-vortex solution. The phase of the deformed vortex obeys the equation

$$\nabla_\parallel^2 \phi_n + \sin\left(\phi_{n+1} - \phi_n\right) - \sin\left(\phi_n - \phi_{n-1}\right) = 0 \quad \text{(A.2)}$$

with the condition $\phi_1(\bar{x}, \bar{u}(\bar{x})) - \phi_0(\bar{x}, \bar{u}(\bar{x})) = \pi$ defining the vortex core and $\bar{u}(\bar{x}) = u(x)/\gamma d$. In the elastic limit $|du/dx| \ll 1$, at distances smaller than the typical wavelength of deformation, the phase can be approximately represented as

$$\phi_n(\bar{x}, \bar{y}) \approx \phi_n^{(0)}\left[\bar{y} - \bar{u}(\bar{x})\right].$$

On the other hand, at large distances, we can use the London approximation in Eq. (A.2) and find the phase using the Fourier transformation. This gives the phase perturbation $\phi^{(1)}(\bar{\mathbf{k}}) = \phi(\bar{\mathbf{k}}) - \phi^{(0)}(\bar{\mathbf{k}})$ in the form

$$\phi^{(1)}(\bar{\mathbf{k}}) \approx \frac{2\pi i \bar{k}_z \bar{u}(\bar{k}_x)}{\bar{k}^2}, \quad \text{(A.3)}$$

where $(\bar{k}_x, \bar{k}_y, \bar{k}_z) = (\gamma dk_x, \gamma dk_y, dk_z)$ and $\bar{k}^2 = \bar{k}_x^2 + \bar{k}_y^2 + \bar{k}_z^2$. We use this result in a mixed $(\bar{k}_x, \bar{y}, \bar{z})$-representation, which is obtained by the inverse Fourier transform of the above equations with respect to $\bar{y}$ and $\bar{z}$,

$$\phi^{(1)}(\bar{\mathbf{r}}, \bar{k}_x) \approx \bar{u}(\bar{k}_x)\nabla_{\bar{z}} K_0(\bar{k}_x \bar{r}) \qquad (A.4)$$

with $\bar{\mathbf{r}} = (\bar{y}, \bar{z})$.

We split the total energy loss given by Eq. (A.1) into the x-gradient and transverse parts, $\delta F = F_x + F_{zy}$. The x-gradient part,

$$F_x = \frac{E_0}{2} \sum_n \int d\bar{x} \int d\bar{y} \left(\nabla_{\bar{x}} \phi_n\right)^2,$$

can be computed by introducing an intermediate scale $1 \ll R \ll 1/\bar{k}_x$ that splits the integral into the two contributions, from small and large distances. The contribution from $\bar{r} = \sqrt{\bar{y}^2 + \bar{z}^2} < R$ with $\bar{z} = n - 1/2$ is given by

$$F_{x,<} \approx \frac{E_0}{2} \int d\bar{x} \left(\frac{du}{d\bar{x}}\right)^2 \sum_n \int\limits_{-y_n}^{y_n} d\bar{y} \left(\nabla_{\bar{y}} \phi_n^{(0)}\right)^2,$$

where $y_n = \sqrt{R^2 - (n-1/2)^2}$. The quantity

$$\sum_n \int\limits_{-y_n}^{y_n} d\bar{y} \left(\nabla_{\bar{y}} \phi_n^{(0)}\right)^2 \approx \frac{\pi}{2}\left(\ln R + C_y\right)$$

is determined by the exact phase distribution in the core. Using the accurate numerical solution, we estimate $C_y \approx 0.93$. The contribution from the region $r > R$ is computed using Eq. (A.4),

$$F_{x,>} \approx \frac{E_0}{2} \int d\bar{x} \int\limits_{\bar{r}>R} d^2\bar{\mathbf{r}} \left(\nabla_{\bar{x}} \phi_n\right)^2 =$$
$$= \frac{E_0}{2} \int \frac{d\bar{k}_x}{2\pi} \bar{k}_x^2 |\bar{u}(\bar{k}_x)|^2 \int\limits_{\bar{r}>R} d^2\bar{\mathbf{r}} \left[\nabla_{\bar{z}} K_0(\bar{k}_x \bar{r})\right]^2.$$

Computing the integral

$$\int\limits_{\bar{r}>R} d^2\bar{\mathbf{r}} \left[\nabla_{\bar{z}} K_0(\bar{k}_x \bar{r})\right]^2 \approx \pi \left(\ln \frac{2}{\bar{k}_x \bar{R}} - \gamma_E - \frac{1}{2}\right),$$

where $\gamma_E \approx 0.5772$ is the Euler constant, we obtain

$$F_{x,>} \approx \frac{\pi}{2} E_0 \int \frac{d\bar{k}_x}{2\pi} \bar{k}_x^2 \left(\ln \frac{2}{\bar{k}_x \bar{R}} - \gamma_E - \frac{1}{2}\right) |\bar{u}(\bar{k}_x)|^2.$$

Combining the parts $F_{x,<}$ and $F_{x,>}$, we obtain

$$F_x = \frac{\pi}{2} E_0 \int \frac{d\bar{k}_x}{2\pi} \bar{k}_x^2 \left(\ln \frac{2}{\bar{k}_x} - \gamma_E - \frac{1}{2} + C_y\right) \times$$
$$\times |\bar{u}(\bar{k}_x)|^2. \qquad (A.5)$$

In the transverse part

$$F_{xy} \approx E_0 \sum_n \int d\bar{x} \int d\bar{y} \times$$
$$\times \left[\frac{1}{2}\left(\nabla_{\bar{y}} \phi_n\right)^2 - \cos\left(\phi_{n+1} - \phi_n\right) - \right.$$
$$\left. - \frac{1}{2}\left(\nabla_{\bar{y}} \phi_n^{(0)}\right)^2 + \cos\left(\phi_{n+1}^{(0)} - \phi_n^{(0)}\right)\right],$$

we replace $\phi_n^{(0)}(\bar{y}, \bar{z})$ with $\phi_n^{(0)}(\bar{y} - \bar{u}(\bar{x}), \bar{z})$ and represent $\phi_n(\bar{x}, \bar{y})$ as $\phi_n(\bar{x}, \bar{y}) = \phi_n^{(0)}(\bar{y} - \bar{u}(\bar{x})) + \tilde{\phi}_n(\bar{x}, \bar{y})$, where the Fourier transform of $\tilde{\phi}_n(\bar{x}, \bar{y})$ at small wave vectors is given by

$$\tilde{\phi}(\bar{\mathbf{k}}) = 2\pi i \left(\frac{1}{\bar{k}^2} - \frac{1}{\bar{k}_y^2 + \bar{k}_z^2}\right) \bar{k}_z \bar{u}(\bar{k}_x) =$$
$$= -\frac{2\pi i \bar{k}_x^2}{\left(\bar{k}_y^2 + \bar{k}_z^2\right)\bar{k}^2} \bar{k}_z \bar{u}(\bar{k}_x).$$

We see in what follows that the main contribution to F_{xy} comes from the distances of the order of a typical wavelength of deformations far away from the core. Therefore, we can expand with respect to $\tilde{\phi}_n$ and can use the linear and continuous approximation

$$F_{yz} \approx \frac{E_0}{2} \int \frac{d^3\bar{\mathbf{k}}}{(2\pi)^3} \left(\bar{k}_y^2 + \bar{k}_z^2\right) |\tilde{\phi}(\bar{\mathbf{k}})|^2.$$

Substituting $\tilde{\phi}(\bar{\mathbf{k}})$ and computing the integral with respect to $\bar{k}_y$ and $\bar{k}_z$, which converges at $\bar{k}_y$, $\bar{k}_z \sim \bar{k}_x$, we obtain

$$F_{yz} \approx \frac{\pi}{4} E_0 \int \frac{d\bar{k}_x}{2\pi} \bar{k}_x^2 |\bar{u}(\bar{k}_x)|^2. \qquad (A.6)$$

Finally, combining (A.5) and (A.6), we obtain the line-tension energy of the Josephson vortex in (31), presented already in the real coordinates with the numerical constant $C_t = 2\exp(-\gamma_E + C_y)$.

APPENDIX B

Discrete and nonlinear corrections to the Josephson vortex phase and energy at large distances from the core

The phase distribution $\phi_n(y)$ in the Josephson vortex core obeys Eq. (20). We measure the in-plane coordinate y in units of the Josephson length $\Lambda_J = \gamma d$ defining the dimensionless coordinate $\bar{y} = y/\gamma d$ and rewrite (20) in the form

$$\frac{d^2\phi_n}{d\bar{y}^2} + \sin\left[\phi_{n+1}(\bar{y}) - \phi_n(\bar{y})\right] +$$
$$+ \sin\left[\phi_{n-1}(\bar{y}) - \phi_n(\bar{y})\right] = 0.$$

At large distances from the core, $n^2 + \bar{y}^2 \gg 1$, this equation transforms into the isotropic London equation $\nabla^2\phi = 0$. In this region, $\phi_n(\bar{y})$ can be approximated by a continuous function $\phi(\bar{y}, \bar{z})$ with $n \to \bar{z}$. Using the Taylor series for the difference $\phi(\bar{y}, \bar{z}+1) - \phi(\bar{y}, \bar{z})$, we obtain

$$\sin[\phi(\bar{y}, \bar{z}+1) - \phi(\bar{y}, \bar{z})] + \\ + \sin[\phi(\bar{y}, \bar{z}-1) - \phi(\bar{y}, \bar{z})] \approx \\ \approx \frac{\partial^2\phi}{\partial\bar{z}^2} + \frac{1}{12}\frac{\partial^4\phi}{\partial\bar{z}^4} - \frac{1}{2}\left(\frac{\partial\phi}{\partial\bar{z}}\right)^2\frac{\partial^2\phi}{\partial\bar{z}^2} + \ldots$$

Therefore, the phase equation to 4th order in the gradient (which is small at large distances) is given by

$$\frac{\partial^2\phi}{\partial\bar{y}^2} + \frac{\partial^2\phi}{\partial\bar{z}^2} + \frac{1}{12}\frac{\partial^4\phi}{\partial\bar{z}^4} - \frac{1}{2}\left(\frac{\partial\phi}{\partial\bar{z}}\right)^2\frac{\partial^2\phi}{\partial\bar{z}^2} = 0. \quad \text{(B.1)}$$

This equation can be solved iteratively. For the Josephson vortex located at $\bar{y} = 0$ in between the layers 0 and 1, the zeroth-order solution ϕ^0 (correct to the second order in the gradients) is given by $\phi^0(\bar{y}, \bar{z}) = -\operatorname{arctg}[(\bar{z} - 1/2)/\bar{y}]$ (we note that for $\bar{z} = n$, we have $\phi^0(y/\gamma d, n) = \phi_n^{Jv}(y)$ in (21)). The first-order correction $\delta\phi^1(\bar{y}, \bar{z})$ obeys the equation

$$\nabla^2\delta\phi^1 = -\frac{1}{12}\frac{\partial^4\phi^0}{\partial\bar{z}^4} + \frac{1}{2}\left(\frac{\partial\phi^0}{\partial\bar{z}}\right)^2\frac{\partial^2\phi^0}{\partial\bar{z}^2} = \\ = \frac{2\sin(2\phi^0) + 5\sin(4\phi^0)}{8\bar{r}^4},$$

where $\bar{r}^2 = \bar{y}^2 + (\bar{z} - 1/2)^2$. Using the solutions of the inhomogeneous Laplace equations

$$\nabla^2\phi = \frac{\sin 2\phi^0}{\bar{r}^4} \to \phi = -\frac{\sin 2\phi^0}{4\bar{r}^2}\ln\bar{r},$$

$$\nabla^2\phi = \frac{\sin 4\phi^0}{\bar{r}^4} \to \phi = -\frac{\sin 4\phi^0}{12\bar{r}^2},$$

we build the solution for $\delta\phi^1(\bar{r}, \phi^0)$ and arrive at the correction

$$\delta\phi(\bar{y}, \bar{z}) = \frac{\sin(2\phi^0)}{16\bar{r}^2}(\ln\bar{r} + C_{\delta\phi}) + \\ + \frac{5\sin(4\phi^0)}{96\bar{r}^2} + \mathcal{O}(1/\bar{r}^4). \quad \text{(B.2)}$$

Here, we have added the solution $\sin(2\phi^0)/\bar{r}^2$ of the homogeneous Laplace equation with an unknown numerical constant $C_{\delta\phi}$. Comparison of these asymptotic expressions with the full numerical solution gives $C_{\delta\phi} \approx 4.362$. The result in (B.2) is given in unscaled coordinates in (28).

In a similar way, we can derive a nonlinear/discrete correction to the energy far away from the core. The reduced energy contribution to the Josephson vortex from the region $\bar{r} < \lambda_{ab}/d$ is given by

$$\varepsilon_{Jv} = \int d\bar{y}\sum_n\left[\frac{1}{2}\left(\frac{d\phi_n}{d\bar{y}}\right)^2 + 1 - \cos(\phi_{n+1} - \phi_n)\right].$$

In the region $\bar{r} \gg 1$, we can again use the expansion with respect to a small gradient along the z axis, which leads to the result

$$\varepsilon_{Jv} \approx \int\limits_{1\ll\bar{r}\ll\lambda_{ab}/d} d^2\bar{\mathbf{r}}\left[\frac{1}{2}\left(\frac{d\phi}{d\bar{y}}\right)^2 + \frac{1}{2}\left(\frac{\partial\phi}{\partial\bar{z}}\right)^2 - \right. \\ \left. - \frac{1}{24}\left(\frac{\partial^2\phi}{\partial\bar{z}^2}\right)^2 - \frac{1}{24}\left(\frac{\partial\phi}{\partial\bar{z}}\right)^4\right].$$

In the lowest order with respect to small gradients, this gives the correction to the energy due to the layered structure

$$\delta\varepsilon_{Jv} = -\frac{1}{24}\times \\ \times \int\limits_{1\ll\bar{\mathbf{r}}\ll\lambda_{ab}/d} d^2\bar{\mathbf{r}}\left[\left(\frac{\partial^2\phi^0}{\partial\bar{z}^2}\right)^2 + \left(\frac{\partial\phi^0}{\partial\bar{z}}\right)^4\right]. \quad \text{(B.3)}$$

In the case of a single Josephson vortex, this formula is not very useful because the integral is formally divergent at small distances and is determined by the small-distance cut-off. In the case of a finite vortex density, however, a generalization of this equation allows obtaining a nontrivial correction to the vortex-lattice energy.

In the vortex-lattice case at a finite in-plane field, following the same reasoning, we obtain the correction to the reduced energy per unit cell in (56):

$$\delta u = \frac{1}{\pi}\int\limits_{u.c.} d^2\bar{\mathbf{r}}\times \\ \times\left[-\frac{1}{24}\left(\frac{\partial^2\phi^0}{\partial\bar{z}^2}\right)^2 - \frac{1}{24}\left(\frac{\partial\phi^0}{\partial\bar{z}} + h\bar{y}\right)^4\right], \quad \text{(B.4)}$$

where integration is performed over the unit cell and $\phi^0(\bar{\mathbf{r}})$ is the vortex-lattice phase within the London approximation. To estimate the dominating contribution, we use the circular-cell approximation for the lattice phase. In this approximation, supercurrents flow radially within the cell $\bar{r} < a_c = \sqrt{2/h}$ and vanish at its boundary, and hence the gauge-invariant phase gradient is given by

$$\frac{1}{\bar{r}}\frac{\partial\phi_{cc}}{\partial\alpha} = -\frac{1}{\bar{r}} + \frac{\bar{r}}{a_c^2} \quad \text{for } 0 < r < a_c,$$

where $\alpha = \mathrm{tg}^{-1}(\bar{z}/\bar{y})$ is the polar angle, whence $\partial\phi^0/\partial\bar{z} + h\bar{y} \to -\cos(\alpha)(1/r - r/a_c^2)$. The integral formally diverges at small distances. This divergence, however, is due to the vortex-core energy. To find the nontrivial correction to the lattice energy, we subtract the diverging single-vortex term. The dominating contribution to the rest part comes from the second (nonlinear) term

$$\delta u \approx -\frac{1}{24\pi}\int\limits_0^{2\pi} d\alpha \times \\ \times \int\limits_0^{a_c} \bar{r}\, d\bar{r}\cos^4(\alpha)\left[\left(\frac{1}{\bar{r}} - \frac{\bar{r}}{a_c^2}\right)^4 - \frac{1}{\bar{r}^4}\right], \quad \text{(B.5)}$$

and calculation gives the result

$$\delta u = \frac{h}{32}\ln\frac{C_h}{h}. \quad \text{(B.6)}$$

From the fit of the numerically computed energy to this formula, we obtain the numerical constant $C_h \approx 110$. We note that this correction does not depend on the lattice orientation with respect to the layers. Interaction with the layers also eliminates the "elliptic" rotation degeneracy of the lattice described in Sec. 4. Expansion (B.5), however, is not sufficient to find the orientation-dependent correction to the energy. To obtain that correction, one has to obtain the next-order expansion with respect to the gradients (6-th order terms).

APPENDIX C

Calculation of the orientation-dependent fluctuation correction to the free energy

In this appendix, we present the calculation of the entropy correction to free energy (98) based on the planar elastic energy (96). To facilitate calculations, we again introduce the reduced wave vectors $\tilde{\mathbf{k}}$ defined in Eq. (90) and the corresponding reciprocal-lattice vectors $\tilde{\mathbf{Q}} = (\tilde{Q}_y, \tilde{Q}_z)$. In this presentation, the reciprocal lattice becomes a regular triangular lattice with the unit vector $Q_0 = \sqrt{2\pi/\sqrt{3}}$ and the area of the Bravais cell is equal to π. Using the new variables, we represent $\Phi_{JVL}(\mathbf{k})$ in the compact reduced form as

$$\Phi_{JVL}(\mathbf{k}) = \frac{B_x^2}{4\pi\lambda_c^2}\phi_{JVL}(\tilde{\mathbf{k}}), \quad \text{(C.1)}$$

$$\phi_{JVL}(\tilde{\mathbf{k}}) = \\ = \sum_{\tilde{\mathbf{Q}}}\left[\frac{\left(\tilde{k}_y - \tilde{Q}_y\right)^2 + \tilde{k}_x^2}{b_x^{-1} + \left(\tilde{\mathbf{k}}_{yz} - \tilde{\mathbf{Q}}\right)^2 + \tilde{k}_x^2} - \frac{\tilde{Q}_y^2}{b_x^{-1} + \tilde{Q}^2}\right], \quad \text{(C.2)}$$

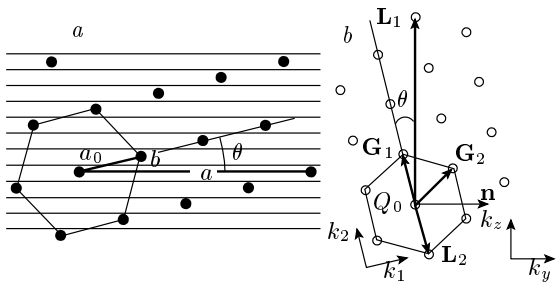

Fig. 18. *a*) Josephson vortex lattice in reduced coordinates rotated at a finite angle θ with respect to the layers in real space such that the layers align with the crystallographic direction $(3,1)$. *b*) The corresponding reciprocal lattice and illustration of two selections for the basis used in the calculation of the entropy correction: the basic wave vectors $\mathbf{G}_{1,2}$ aligned with the lattice, and the basic wave vectors $\mathbf{L}_{1,2}$ aligned with the layers

where $b_x = 4\pi\lambda_{ab}\lambda_c B_x/\Phi_0 = 2\,(\lambda_{ab}/d)^2\, h \gg 1$ and $\tilde{\mathbf{k}}_{yz} = (0, \tilde{k}_y, \tilde{k}_z)$.

We assume that the lattice is rotated at a finite angle θ with respect to the layers selected in such a way that the layers are aligned with one of the crystallographic directions, as sketched in Fig. 18. This means that the lattice, in general, has the form of a misaligned lattice sketched in Fig. 6*a* and is characterized by the aspect ratio $r = \gamma b/a$ and the shift parameter, q. To compute the sum over the reciprocal-lattice vectors, we use two equivalent parameterizations illustrated in Fig. 18. The first parameterization uses an expansion over the two basic vector of the tilted lattice, $\tilde{\mathbf{Q}} = n\mathbf{G}_1 + m\mathbf{G}_2$ with $m, n = 0, \pm 1, \pm 2\ldots$ For such an expansion, we can simply represent the component of $\tilde{\mathbf{Q}}$ along the two main directions of the tilted lattice, $(\mathbf{k}_1, \mathbf{k}_2)$, shown in Fig. 18,

$$\tilde{Q}_1 = \frac{\sqrt{3}}{2}mQ_0, \quad \tilde{Q}_2 = \left(n + \frac{m}{2}\right)Q_0. \quad \text{(C.3)}$$

This gives $\tilde{Q}^2 = \left(n^2 + nm + m^2\right)Q_0^2$. The (y,z) components of the wave vectors are related to the $(1,2)$ components by axis rotation. For example, for the component $\tilde{k}_y$ in Eq. (C.2), we have $\tilde{k}_y = \cos\theta\tilde{k}_1 + \sin\theta\tilde{k}_2$. This parameterization allows us to naturally trace the dependence on the rotation angle θ. The second parameterization utilizes the basic wave vectors aligned with the layers,

$$\tilde{\mathbf{Q}} = n\mathbf{L}_1 + m\mathbf{L}_2, \\ \mathbf{L}_1 = \left(0, \sqrt{\frac{\pi}{r}}\right), \quad \mathbf{L}_2 = \left(\sqrt{\pi r}, -q\sqrt{\frac{\pi}{r}}\right). \quad \text{(C.4)}$$

This basis allows easily tracing the dependence on the lattice-structure parameters r and q. It also allows reducing $\phi_{JVL}(\tilde{\mathbf{k}})$ to a simpler form. Substituting presentation (C.4) in Eq. (C.2) and taking the sum over n, we obtain

$$\phi_{JVL}(\tilde{\mathbf{k}}) = \sqrt{\pi r}\sum_{m=-\infty}^{\infty}\left(\frac{\left(\tilde{k}_y - m\sqrt{\pi r}\right)^2 + \tilde{k}_x^2}{\kappa(\tilde{k}_y - m\sqrt{\pi r}, \tilde{k}_x)} \times \right.$$

$$\times \frac{\operatorname{sh}\left[2\sqrt{\pi r}\kappa(\tilde{k}_y - m\sqrt{\pi r}, \tilde{k}_x)\right]}{\operatorname{ch}\left[2\sqrt{\pi r}\kappa(\tilde{k}_y - m\sqrt{\pi r}, \tilde{k}_x)\right] - \cos\left[2\pi\left(qm + \tilde{k}_z\sqrt{\frac{r}{\pi}}\right)\right]} -$$

$$\left. - \frac{\pi r m^2}{\kappa(m\sqrt{\pi r}, 0)} \frac{\operatorname{sh}\left[2\sqrt{\pi r}\kappa(m\sqrt{\pi r}, 0)\right]}{\operatorname{ch}\left[2\sqrt{\pi r}\kappa(m\sqrt{\pi r}, 0)\right] - \cos(2\pi q m)}\right)$$

with $\kappa(k_y, k_x) \equiv \sqrt{b_x^{-1} + k_y^2 + k_x^2}$. This formula contains only one summation, which makes it convenient for numerical evaluations. On the other hand, the dependence on the rotation angle here is not obvious and is hidden in the dependence on the parameters r and q.

The sums over the reciprocal-lattice vectors in Eqs. (97) and (C.2) formally diverge logarithmically at large $\mathbf{Q}$ ($\tilde{\mathbf{Q}}$). Correspondingly, the sum over m in Eq. (C.5) also logarithmically diverges. This divergence is due to the single-vortex tilt energy and has to be cut at the core size, $Q_y \sim 1/\gamma d$. This energy was considered in details in Sec. 3.1. We split the reduced elastic matrix $\phi_{JVL}(\tilde{\mathbf{k}})$ into the single-vortex, $\phi_{sv}(\tilde{k}_x)$, and interaction, $\phi_i(\tilde{\mathbf{k}})$, terms,

$$\phi_{JVL}(\tilde{\mathbf{k}}) = \phi_{sv}(\tilde{k}_x) + \phi_i(\tilde{\mathbf{k}}).$$

The single-vortex term $\phi_{sv}(\tilde{k}_x)$ can be obtained from Eq. (C.2) by replacing the summation over $\tilde{\mathbf{Q}}$ with integration,

$$\phi_{sv}(\tilde{k}_x) = \int \frac{d^2\tilde{\mathbf{Q}}}{\pi}\left[\frac{\tilde{Q}_y^2 + \tilde{k}_x^2}{b_x^{-1} + \tilde{\mathbf{Q}}^2 + \tilde{k}_x^2} - \frac{\tilde{Q}_y^2}{b_x^{-1} + \tilde{\mathbf{Q}}^2}\right].$$

Using Eq. (31), we obtain the line-tension term in real units, $\Phi_{sv}(k_x) = \pi(B_x/\Phi_0)\varepsilon_J k_x^2 \ln(C_t/\gamma d k_x)$ with $\varepsilon_J \equiv E_0/\gamma d$ and $C_t \approx 2.86$. This corresponds to the following result for the reduced line-tension term $\phi_{sv}(\tilde{k}_x) = \left(4\pi\lambda_c^2/B_x^2\right)\Phi_{sv}(k_x)$:

$$\phi_{sv}(\tilde{k}_x) \approx \frac{\tilde{k}_x^2}{2}\ln\frac{4.09}{h\tilde{k}_x^2} \qquad \text{(C.5)}$$

for $\tilde{k}_x^2 \ll 4/h$. In the interaction term $\phi_i(\tilde{\mathbf{k}}) = \phi_{JVL}(\tilde{\mathbf{k}}) - \phi_{sv}(\tilde{k}_x)$, the logarithmic divergence is compensated and the sum over $\tilde{\mathbf{Q}}$ converges roughly at $\tilde{Q} \sim 1$. In particular, using the presentation in (C.5), the interaction term can be represented as a converging sum,

$$\phi_i(\mathbf{k}) = \sqrt{\pi r}\sum_{m=-\infty}^{\infty}\left(\frac{\left(\tilde{k}_y - m\sqrt{\pi r}\right)^2 + \tilde{k}_x^2}{\kappa(\tilde{k}_y - m\sqrt{\pi r}, \tilde{k}_x)} \frac{\operatorname{sh}\left[2\sqrt{\pi r}\kappa(\tilde{k}_y - m\sqrt{\pi r}, \tilde{k}_x)\right]}{\operatorname{ch}\left[2\sqrt{\pi r}\kappa(\tilde{k}_y - m\sqrt{\pi r}, \tilde{k}_x)\right] - \cos\left[2\pi\left(qm + \tilde{k}_z\sqrt{\frac{r}{\pi}}\right)\right]} -\right.$$

$$- \sum_{\delta=\pm1}\delta\; U\left[\tilde{k}_x, (m+\delta/2)\sqrt{\pi r} - \tilde{k}_y\right] -$$

$$\left. - \frac{\pi r m^2}{\kappa(m\sqrt{\pi r}, 0)} \frac{\operatorname{sh}\left[2\sqrt{\pi r}\kappa(m\sqrt{\pi r}, 0)\right]}{\operatorname{ch}[2\sqrt{\pi r}\kappa(m\sqrt{\pi r}, 0)] - \cos(2\pi q m)} + \sum_{\delta=\pm1}\delta\; U\left[0, (m+\delta/2)\sqrt{\pi r}\right]\right)$$

with

$$U\,[k_x,k_y] \equiv \frac{1}{2}\left[k_y\sqrt{b_x^{-1}+k_x^2+k_y^2}\,+\right.$$
$$\left.+\,\left(-b_x^{-1}+k_x^2\right)\ln\left(k_y+\sqrt{b_x^{-1}+k_x^2+k_y^2}\right)\right].$$

Here, the terms with $U\,[\ldots,\ldots]$ originate from the single-vortex contribution $\phi_{sv}(\tilde{k}_x)$, which is properly decomposed to compensate the summation divergence. In spite of its scary look, this formula is the most suitable one for numerical calculations.

From Eq. (98), we obtain the entropy correction to the free energy in reduced form

$$\delta f_T = -\frac{T}{2\sqrt{\gamma}}\left(\frac{4\pi B_x}{\Phi_0}\right)^{3/2}\times$$
$$\times\int\limits_{-\infty}^{\infty}\frac{d\tilde{k}_x}{2\pi}\int\limits_{BZ}\frac{d\tilde{k}_y d\tilde{k}_z}{(2\pi)^2}\ln\frac{\tilde{C}}{\phi_{JVL}(\tilde{\mathbf{k}})}, \quad \text{(C.6)}$$

where $\int_{BZ}\ldots$ denotes the integral over the Brillouin zone and $\tilde{C}$ is a dimensionless constant. The integral over k_x is formally diverging. This divergence is due to short-wavelength excitations in the vortex cores and does not contribute to the angular-dependent correction. To separate the regular anisotropic correction, we subtract the isotropic single-vortex contribution from the total free energy and represent the resulting anisotropic correction as

$$\delta f_{T,a}(\theta) = -\frac{T}{\sqrt{\pi\gamma}}\left(\frac{B_x}{\Phi_0}\right)^{3/2} g_a \quad \text{(C.7)}$$

with

$$g_a = \int\limits_{BZ}\frac{d^2\tilde{\mathbf{k}}_{yz}}{\pi}\int\limits_0^{\infty} dk_x \ln\frac{\phi_{sv}(\tilde{k}_x)}{\phi_{sv}(\tilde{k}_x)+\phi_i(\tilde{\mathbf{k}})}. \quad \text{(C.8)}$$

This presentation is used in Eq. (99).

The large logarithmic factor in $\phi_{sv}(\tilde{k}_x)$ in Eq. (C.5) allows obtaining a useful approximate formula for g_a. As $\phi_i(\tilde{\mathbf{k}}) \sim 1$, the integral over $\tilde{k}_x$ converges at $\tilde{k}_x \sim 1/\sqrt{\ln(1/h)} \ll 1$, meaning that for a log-accuracy estimate, we can neglect the $\tilde{k}_x$-dependence of $\phi_i(\tilde{\mathbf{k}})$. Evaluating the integral over k_x, we obtain

$$g_a \approx -\frac{\sqrt{2}}{\sqrt{\ln(A/h)}}\int\limits_{BZ} d^2\tilde{\mathbf{k}}_{yz}\sqrt{\phi_i(\tilde{\mathbf{k}}_{yz})} \quad \text{(C.9)}$$

with $A \sim 1$. If we neglect the small parameter b_x^{-1} in $\phi_i(\tilde{\mathbf{k}}_{yz})$, then the integral in this formula becomes field independent and the only field dependence of g_a for $h \to 0$ is given by the factor $[\ln(A/h)]^{-1/2}$.

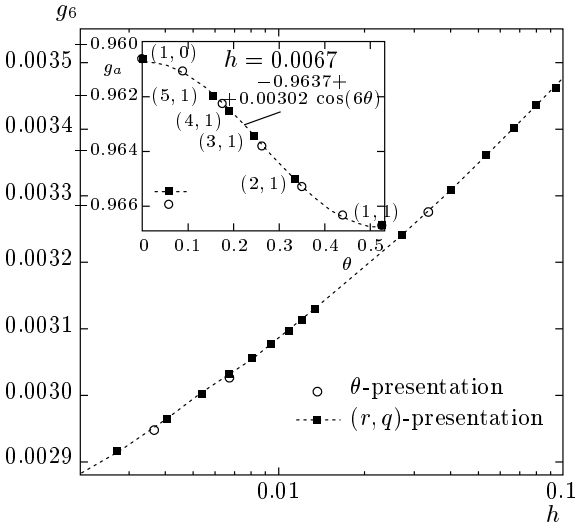

Fig. 19. The inset shows an example of the numerically computed angular dependence of the reduced entropy correction $g_a(\theta)$ defined by Eq. (C.8) for $h = 0.0067$. Solid squares show results obtained using the representation for fixed lattice parameters r and q in Eq. (C.6). This computation is done for layers oriented along the crystal directions (m, n), which are also shown in the plot. Open symbols are obtained using the representation with the explicit dependence on the lattice rotation angle θ using expansion (C.3). The dashed line is the fit to the formula $g_0 + g_6\cos(6\theta)$. The main plot shows the field dependence of the coefficient g_6 and the corresponding fit in Eq. (100)

We numerically computed the reduced entropy correction g_a for different lattice orientations and reduced fields h. An example of the angular dependence of g_a for $h = 0.0067$ is shown in the inset of Fig. 19. We found that in the range $0.001 < h < 0.1$, the orientation-dependent part of g_a can be well fitted by formula (100). The dependence $g_6(h)$ is plotted in Fig. 19. The positive sign of $g_6(h)$ means that the fluctuations give the largest negative contribution at $\theta = 0$, i. e., they indeed favor the aligned lattice (1,0). We also can see that the effect occurs to be quantitatively rather small, at least in the considered Gaussian-fluctuation regime.

REFERENCES

1. B. D. Josephson, Phys. Lett. **1**, 251 (1962).

2. J. G. Bednorz and K. A. Muller, Z. Phys. B **64**, 189 (1986).

3. M. K. Wu, J. R. Ashburn, C. J. Torng et al., Phys. Rev. Lett. **58**, 908 (1987).

4. H. Maeda, Y. Tanaka, M. Fukutomi, and T. Asano, Jpn. J. Appl. Phys. **27**, L209 (1988).

5. C. W. Chu, J. Bechtold, L. Gao et al., Phys. Rev. Lett. **60**, 941 (1988).

6. J. Wilson and A. Yoffe, Adv. in Phys. **18**, 193 (1969).

7. L. N. Bulaevskii, Usp. Fiz. Nauk **116**, 449 (1975).

8. T. Ishiguro and K. Yamaji, *Organic Superconductors*, Springer, Berlin (1990), Ch. 5.

9. J. Singleton, Rep. Prog. Phys. **63**, 1111 (2000).

10. Y. Kamihara, T. Watanabe, M. Hirano, and H. Hosono, J. Amer. Chem. Soc. **130**, 3296 (2008).

11. D. C. Johnston, Adv. in Phys. **59**, 803 (2010).

12. P. C. Canfield and S. L. Bud'ko, Ann. Rev. Cond. Mat. Phys. **1**, 27 (2010).

13. G. R. Stewart, Rev. Mod. Phys. **83**, 1589 (2011).

14. X. H. Chen, T. Wu, G. Wu et al., Nature **453**, 761 (2008).

15. P. J. W. Moll, L. Balicas, V. Geshkenbein et al., Nature Mater. **12**, 134 (2013).

16. X. Zhu, F. Han, G. Mu et al., Phys. Rev. B **79**, 220512 (2009).

17. H. Ogino, Y. Matsumura, Y. Katsura et al., Supercond. Sci. Technol. **22**, 075008 (2009).

18. S. Sato, H. Ogino, N. Kawaguchi et al., Supercond. Sci. Technol. **23**, 045001 (2010).

19. G. Blatter, M. V. Feigelman, V. B. Geshkenbein, A. I. Larkin, and V. M. Vinokur, Rev. Mod. Phys. **66**, 1125 (1994).

20. D. Feinberg, J. Phys. III **4**, 169 (1994).

21. E. H. Brandt, Rep. Prog. Phys. **58**, 1465 (1995).

22. T. Nattermann and S. Scheidl, Adv. Phys. **49**, 607 (2000).

23. G. Blatter and V. B. Geshkenbein, in *The Physics of Superconductors, Vol. 1: Conventional and High-T_c Superconductors*, ed. by K. Bennemann and J. Ketterson, Springer, Berlin (2003), p. 726.

24. L. J. Campbell, M. M. Doria, and V. G. Kogan, Phys. Rev. B **38**, 2439 (1988).

25. L. Bulaevskii and J. R. Clem, Phys. Rev. B **44**, 10234 (1991).

26. J. R. Clem, J. Supercond. **17**, 613 (2004).

27. G. J. Dolan, F. Holtzberg, C. Feild, and T. R. Dinger, Phys. Rev. Lett. **62**, 2184 (1989).

28. M. Oussena, P. A. J. de Groot, R. Gagnon, and L. Taillefer, Phys. Rev. Lett. **72**, 3606 (1994).

29. A. A. Zhukov, H. Küpfer, G. K. Perkins et al., Phys. Rev. B **59**, 11213 (1999).

30. S. N. Gordeev, A. A. Zhukov, P. A. J. de Groot et al., Phys. Rev. Lett. **85**, 4594 (2000).

31. C. A. Bolle, P. L. Gammel, D. G. Grier et al., Phys. Rev. Lett. **66**, 112 (1991).

32. M. Tokunaga, T. Tamegai, Y. Fasano, and F. de la Cruz, Phys. Rev. B **67**, 134501 (2003).

33. A. Grigorenko, S. Bending, T. Tamegai, S. Ooi, and M. Henini, Nature **414**, 728 (2001).

34. T. Matsuda, O. Kamimura, H. Kasai et al., Science **294**, 2136 (2001).

35. A. Tonomura, H. Kasai, O. Kamimura et al., Phys. Rev. Lett. **88**, 237001 (2002).

36. V. K. Vlasko-Vlasov, A. Koshelev, U. Welp, G. W. Crabtree, and K. Kadowaki, Phys. Rev. B **66**, 014523 (2002); in *Proc. NATO Advanced Research Workshop on Magneto-Optical Imaging (Oystese, Norway, Aug. 2003)*, Vol. 142, ed. by T. H. Johansen and D. V. Shantsev, Kluwer Academic, Dordrecht (2002), p. 39.

37. M. Tokunaga, M. Kobayashi, Y. Tokunaga, and T. Tamegai, Phys. Rev. B **66**, 060507 (2002).

38. S. J. Bending and M. J. W. Dodgson, J. Phys.: Condens. Matt. **17**, R955 (2005).

39. J. U. Lee, J. E. Nordman, and G. Hohenwarter, Appl. Phys. Lett. **67**, 1471 (1995); J. U. Lee, P. Guptasarma, D. Hornbaker, A. El-Kortas, D. Hinks, and K. E. Gray, **71**, 1412 (1997).

40. G. Hechtfischer, R. Kleiner, A. V. Ustinov, and P. Müller, Phys. Rev. Lett. **79**, 1365 (1997); G. Hechtfischer, R. Kleiner, K. Schlenga et al., Phys. Rev. B **55**, 14638 (1997).

41. Y. I. Latyshev, M. B. Gaifullin, T. Yamashita, M. Machida, and Y. Matsuda, Phys. Rev. Lett. **87**, 247007 (2001).

42. Y. I. Latyshev, A. E. Koshelev, and L. N. Bulaevskii, Phys. Rev. B **68**, 134504 (2003).

43. S. M. Kim, H. B. Wang, T. Hatano et al., Phys. Rev. B **72**, 140504 (2005).

44. S. Ooi, T. Mochiku, and K. Hirata, Phys. Rev. Lett. **89**, 247002 (2002).

45. B. Y. Zhu, H. B. Wang, S. M. Kim et al., Phys. Rev. B **72**, 174514 (2005).

46. Y. Latyshev, V. Pavlenko, A. P. Orlov, and X. Hu, Pis'ma v ZhETF **82**, 251 (2005).

47. S. O. Katterwe and V. M. Krasnov, Phys. Rev. B **80**, 020502 (2009).

48. I. Kakeya, Y. Kubo, M. Kohri et al., Phys. Rev. B **79**, 212503 (2009).

49. W. E. Lawrence and S. Doniach, in *Proc. 12th Int. Conf. Low Temp. Phys.*, Kyoto, Japan, ed. by E. Kanda (1970), p. 361.

50. L. N. Bulaevskii, Zh. Eksp. Teor. Fiz. **64**, 2241 (1973).

51. B. D. Josephson, Adv. Phys. **14**, 419 (1965).

52. J. R. Clem and M. Coffey, Phys. Rev. B **42**, 6209 (1990).

53. A. E. Koshelev, Phys. Rev. B **48**, 1180 (1993).

54. J. R. Clem, M. W. Coffey, and Z. Hao, Phys. Rev. B **44**, 2732 (1991).

55. R. A. Klemm and J. R. Clem, Phys. Rev. B **21**, 1868 (1980).

56. G. Blatter, V. B. Geshkenbein, and A. I. Larkin, Phys. Rev. Lett. **68**, 875 (1992).

57. B. I. Ivlev, N. B. Kopnin, and V. L. Pokrovskii, J. Low Temp. Phys. **80**, 187 (1990).

58. L. S. Levitov, Phys. Rev. Lett. **66**, 224 (1992).

59. M. F. Laguna, D. Dominguez, and C. A. Balseiro, Phys. Rev. B **62**, 6692 (2000).

60. B. M. Stewart, *Theory of Numbers*, The Macmillan Company, New York (1964).

61. M. Ichioka, Phys. Rev. B **51**, 9423 (1995).

62. A. E. Koshelev, Proceedings of FIMS/ITSNS/CTC/ /PLASMA 2004, Tsukuba, Japan, Nov. 2428, 2004; arXiv:cond-mat/0602341.

63. Y. Nonomura and X. Hu, Phys. Rev. B **74**, 024504 (2006).

64. R. Ikeda and K. Isotani, J. Phys. Soc. Jpn. **68**, 599 (1999).

65. S. E. Korshunov, Europhys. Lett. **15**, 771 (1990).

66. S. E. Korshunov and A. I. Larkin, Phys. Rev. B **46**, 6395 (1992).

67. A. E. Koshelev, Phys. Rev. B **66**, 224514 (2002); **75**, 214513 (2007).

68. M. Machida, Phys. Rev. Lett. **90**, 037001 (2003); **96**, 097002 (2006).

69. A. Irie and G. Oya, Supercond. Sci. Technol. **20**, S18 (2007).

70. K. B. Efetov, Zh. Eksp. Teor. Fiz. **76**, 1781 (1979).

71. B. Horovitz, Phys. Rev. B **47**, 5964 (1993).

72. L. Balents and D. R. Nelson, Phys. Rev. B **52**, 12951 (1995).

73. L. Balents and L. Radzihovsky, Phys. Rev. Lett. **76**, 3416 (1996).

74. X. Hu, M. Luo, and Y. Ma, Phys. Rev. B **72**, 174503 (2005).

75. X. Hu and M. Tachiki, Phys. Rev. Lett. **85**, 2577 (2000).

76. X. Hu and M. Tachiki, Phys. Rev. B **70**, 064506 (2004).

77. A. E. Koshelev, Phys. Rev. B **50**, 506 (1994).

78. W. K. Kwok, J. Fendrich, U. Welp et al., Phys. Rev. Lett. **72**, 1088 (1994).

79. J. Villain, R. Bidaux, J. Carton, and R. Conte, J. de Phys. **41**, 1263 (1980).

80. V. L. Pokrovskii and G. V. Uimin, Zh. Eksp. Teor. Fiz. **65**, 1961 (1973).

81. L. I. Glazman and A. E. Koshelev, Zh. Eksp. Teor. Fiz. **97**, 1371 (1990).

82. R. A. Ferrell and R. E. Prange, Phys. Rev. Lett. **10**, 479 (1963).